Para aminosalicylic acid in the treatment of manganese toxicity.

Complexation of Mn^{2+} with 4-amino-2-hydroxybenzoic acid and its N-acetylated metabolite.

Joanna Izabela Lachowicz[a*], Valeria Marina Nurchi[a], Guido Crisponi[a], Ilaria Cappai, Rosita Cappai[a], Matteo Busato[b], Andrea Melchior[b], Marilena Tolazzi[b], Massimiliano Peana[c], Eugenio Garribba[c], Maria Antonietta Zoroddu[c], Pierpaolo Coni[d], Giuseppina Pichiri[d], Jan Aaseth[e]

[a]Dipartimento di Scienze Chimiche e Geologiche, Università di Cagliari, Cittadella Universitaria, I-09042 Monserrato, Cagliari, Italy

[b]DPIA, Laboratorio di Scienze e Tecnologie Chimiche, Università di Udine, Via del Cotonificio 108, 33100 Udine, Italy

[c]Dipartimento di Chimica e Farmacia, Università di Sassari, Via Vienna 2, 07100 Sassari, Italy

[d]Dipartimento di Scienze Chirurgiche, Università di Cagliari, Cittadella Universitaria, I-09042 Monserrato, Cagliari, Italy

[e] Department of Public Health, Hedmark University College, Elverum; Department of Internal Medicine, Innlandet Hospital, Kongsvinger, Hedmark, Norway

Corresponding author: Joanna Izabela Lachowicz, Dipartimento di Scienze Chimiche e Geologiche, Cittadella Universitaria, 09042 Monserrato-Cagliari.
Phone +39 070 675 4471   Fax +39 070 675 4478   email: lachowicz@unica.it

Abstract

Manganese excess can induce in humans neurological disorders known as manganism. A possible remedy should be chelation therapy, even if a chelation schedule for manganism is not currently established. Para aminosalicylic acid (PAS) has demonstrated effectiveness in reducing manganism symptoms. In this work, a study of protonation equilibria of para aminosalicylic acid and of its N-acetylated metabolite (Ac-PAS) and of their complexation reactions with Mn^{2+} is presented, also extended to the main essential metal ions Cu^{2+} and Fe^{3+}. A number of complementary techniques (potentiometry, spectrophotometry, fluorimetry, EPR) have been used for a thorough comprehension of protonation and complex formation equilibria, with the addition of DFT calculations, which provide

1

insights on the relative stabilities and electronic properties of the formed species. Both PAS and Ac-PAS form 1:1 and 1:2 metal:ligand complexes with the target Mn^{2+} ion; surprisingly the N-acetylated metabolite forms stronger complexes, whose implications in chelation therapy have been pointed out by a speciation study. It is presumed that the relatively small metabolite can penetrate across the blood-brain-barrier and exert its Mn-mobilizing action intracellularly in vulnerable neurons.

Introduction

The trace element manganese is an essential metal ion, whose dietary deficiency can cause a wide variety of health problems [1]. It is indispensable for the normal development and for the body function of all mammals, since it regulates many enzymes throughout the body [2-4]. Manganese excess associated with occupational and environmental exposure can induce acute effects and/or neurological disorders with a syndrome known as manganism, similar for a number of symptoms to Parkinson's disease. The main cause of manganese toxicity is inhalation, especially when air content is greater than 5 mg m^{-3} and particulate size is less than 5µm [5-7].

A possible remedy against manganism should be chelation therapy, even if currently "*a chelation schedule in chronic manganese poisoning (manganism) is not established, but diethylenetriaminepentaacetic acid (DTPA), ethylenediaminetetraacetic acid (EDTA), and para-aminosalicylic acid (PAS) are available as potential chelators. PAS appears to be the most promising agent, although clinical experience is limited"*, as reported by Andersen in a detailed review of the literature related to experimental and clinical chelation studies [8]. While DTPA and EDTA seems to lack of efficacy in the clinical treatment of manganism, PAS has demonstrated effectiveness in reducing manganism symptoms in its use in China. Shuqin et al. report two cases of chronic manganese poisoning efficaciously treated with PAS (previous treatments with CaNa$_2$EDTA gave initially an improvement of symptoms, which emerged again and became more aggravated daily) [9]. Jiang et al. present an analogous case of PAS treatment of a woman aged 50 for occupational manganism, and followed then at the age of 67 years, i.e. 17 years after the treatment [10]. The examination showed a general normal appearance in clinical, neurological and brain NMR imaging presentations. In the same reference [10] a Table reports on 85 successful treatments of manganism with PAS, and this led the authors to assert that this drug appears effective for treating manganese intoxications. The high dosage of PAS in these treatments has to be remarked: a solution of 500 mL of 10% glucose and 6 g of sodium PAS was given intravenously per day. Each course of intermittent treatment - four days on the drug alternating with three days without the drug - was extended for 3.5 months.

PAS is a second line agent in use for multidrug-resistant tuberculosis; a granule formulation of PAS has been approved in 1995 by US FDA, and PAS combined with other antibiotics is also used against cerebral manifestations of tuberculosis. The recommended daily oral prescription is 8-12 g given in 2-3 doses. PAS was also defined by US FDA as an orphan drug in the treatment of Crohn's disease, since it also exerts an anti-inflammatory action resembling that of aspirin (acetyl salicylic acid).

Two pharmacokinetic studies on PAS can be found in the literature. The first, on humans, is relative to the oral administration of granules [11], and the second, on rats, was designed to investigate the pharmacokinetics and the bio-distribution in the brain [12]. Both articles give evidence of the formation of a N-acetylated metabolite of PAS (AcPAS), and in particular Hong et al. [12] state that PAS and AcPAS seem to be both effective in reducing manganese levels in brain.

Based on all these reports, it seemed necessary to study the protonation equilibria of PAS and AcPAS (Scheme 1) and their complex formation with the target Mn^{2+} metal ion. Salicylic acid was also taken into account for comparison, and the study was extended to the essential Cu^{2+} and Fe^{3+} ions, whose homeostatic equilibria in brain seem to be perturbed by a Mn^{2+} ion excess [13]. Complementary techniques (potentiometry, UV-Vis, EPR spectroscopy and spectrofluorimetry) were used to define the equilibria and the possible nature of the species formed. Computational calculations on the ligands and their Mn^{2+} complexes have been also run in order to provide additional insights on geometry, relative stability and electronic properties of the species.
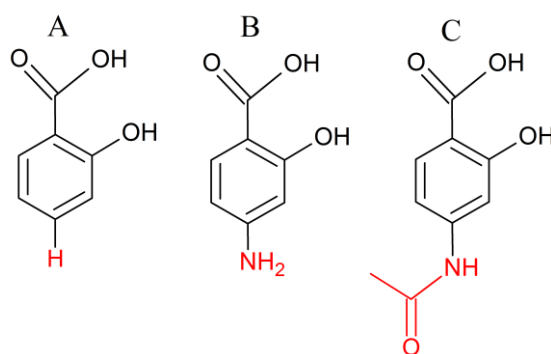
Scheme 1. Molecular structures of (A) 2-hydroxybenzoic acid (SAL), (B) 4-amino-2-hydroxybenzoic acid (PAS), and (C) 4-(acetylamino)-2-hydroxybenzoic acid (Ac-PAS). The characterizing substituents are marked in red.

2. Experimental

2.1. Reagents

2-hydroxybenzoic acid, 4-aminobenzoic acid, 4-amino-2-hydroxybenzoic acid, $CuCl_2$, $MnCl_2$, $FeCl_3$, NaOH, NaCl, HCl, anhydrous sodium sulfate, ethyl acetate, acetic anhydride, hexane, CD_3OD were purchased from Sigma Aldrich. All the reagents, analytical grade, were used without further purification.

2.2. Synthesis of 4-(acetylamino)-2-hydroxybenzoic acid.

4-(acetylamino)-2-hydroxybenzoic acid was synthesized according to the procedure described by Bade et al. [14], obtaining the pure AcPAS with a 40% yield. ^{1}H-NMR (in CD_3OD) δ 7.96, 7.86 (d, H) 7.31 (s, H), 7.03, 7.01 (d, H) 3.32 (s, 3H).

2.3. Potentiometry

Protonation and complex formation equilibrium studies were carried out under Argon flow in a thermostatted glass cell equipped with a magnetic stirrer. The potentiometric apparatus consisted in Metrohm 691 pH-meter, Dosimat 665 Metrohm titrator and Metrohm LL UNITRODE glass electrode. The titrations were performed in water at 25.0 °C and 0.1 M NaCl ionic strength using 0.1 M NaOH. The electrode was daily calibrated for hydrogen ion concentration by titrating HCl with NaOH using the same experimental conditions as above, and the results were analyzed using the Gran procedure [15]. Working ligand concentration was 0.5 mM both for protonation and for complex formation titrations. Fresh PAS solutions were daily prepared to avoid the decarboxylation process [16]. The metal complex formation equilibria were studied in 1:5 metal/ligand molar ratio. The obtained potentiometric data were processed by Hyperquad 2013 program [17].

2.4. Spectrophotometry

A Varian Cary 50 UV/Vis Spectrophotometer was used for UV–Vis studies. Protonation and iron complex formation equilibria were studied by titrating 20 mL of 0.5 mM ligand solutions with 0.1 M NaOH at 0.1 M NaCl ionic strength, with the use of joined potentiometric spectrophotometric titrations [18]. Spectra for protonation equilibria were recorded in the 200–400 nm spectral range with a 0.2 cm path length fiber-optic probe, for complex formation equilibria in the 350–800 nm spectral range with a 1.0 cm path length fiber-optic probe. The obtained data were processed by HypSpec program [19]. The formation equilibria were also studied in the 0–2 pH range on sets of solutions at variable molar concentrations of hydrochloric acid, since complex formation was almost complete when Fe^{3+} and ligand solutions were mixed.

2.5. Spectrofluorimetry

A Varian Cary Fluorimeter was used for fluorescence spectra. Working ligand concentration for the study of protonation equilibria was 0.0125 mM in water. Batch measurements at variable pH were performed by adding proper amounts of HCl and NaOH. The excitation wavelength was 276 nm, while emission spectra were registered in the 286–486 nm spectral range.

2.6. EPR spectroscopy

EPR spectra were recorded from 0 to 10000 Gauss at 120 and 298 K with an X-Band Bruker EMX spectrometer equipped with a HP 53150A microwave frequency counter. The microwave frequency used was in the range 9.40 - 9.43 GHz.

2.7 Computational details

The geometries of the salicylic acid derivatives in the different protonation states have been optimized using the CAM-B3LYP functional [20] with the gaussian-type 6-31+G(d,p) basis set for all the atoms. The time-dependent DFT calculations with the CAM-B3LYP functional, in combination with the selected basis set, have been previously demonstrated to provide electronic excitation spectra for benzoic acid derivatives at different pH values in good agreement with the experimental ones [21] [22]. The spectra were calculated for 24 singlet excitations and applying a 15 nm half-height line broadening. All calculations (geometry optimizations and electronic excitations) were carried out in presence of water as solvent introduced by the PCM method [23].

For the calculations carried out for MnL and $[MnL_2]^{2-}$ complexes (L = SAL, PAS, AcPAS), the B3LYP hybrid functional [24, 25] was chosen as it is widely demonstrated to provide good structural data for metal complexes, especially for open shell systems [26-34]. The Stuttgart-Dresden effective-core potentials [30] with the associated basis set for the valence electrons were employed for Mn within the gaussian-type 6-31+G(d,p) for the other elements. Geometry optimizations for the complexes were carried out both in gas phase and in presence of water introduced by the CPCM solvation model [31, 32]. To assess the dependence of the calculated parameters from the basis set, optimizations with the B3LYP [Y. Zhao, D. G. Truhlar, Theor Chem Account (2008) 120:215–241] functional were also carried out with the 6-31+G(d,p) basis set for all the atoms. Then, the energies were also calculated with the 6-311+G(d,p) and the aug-cc-pVTZ basis sets [T.H. Dunning, Jr. J. Chem. Phys. 90, 1007 (1989); N.B.

Balabanov and K.A. Peterson, J. Chem. Phys, 123, 064107 (2005)]. An additional energy calculation with the SMD solvation model [Marenich, A. V.; Cramer, C. J.; Truhlar, D. G., J. Phys. Chem. B. 2009, 113, 6378–6396] was employed to compare the results with the CPCM. Finally, the M06 functional, which was previously demonstrated to provide accurate structural and thermodynamic data especially for transition metal complexes [Y. Zhao, D. G. Truhlar, Theor Chem Account (2008) 120:215–241; Y. Zhao, D. G. Truhlar, Chemical Physics Letters 502 (2011) 1–13; M. Nardirossian, M. Head-Gordon, J. Chem. Theory Comput. 2016, 12, 4303−4325].[Marenich, A. V.; Cramer, C. J.; Truhlar, D. G., J. Phys. Chem. B. 2009, 113, 6378–6396] was tested with the 6-31+G(d,p) basis set.

According to the results from the EPR analysis (section 3.2), the Mn^{2+} ion has been considered to be in a high spin state (S = 5/2) and the calculations were carried out from starting structures with the metal as octahedral coordinated. In a first geometry optimization, the 1:1 MnL complexes were represented as $Mn(H_2O)_4L$ with one bidentate L ligand and four coordinating water molecules, while the 1:2 $[MnL_2]^{2-}$ species as $[Mn(H_2O)_2L_2]^{2-}$ with two equatorial chelating L ligands and two apical water molecules. However, the minimum structures obtained presented either large distortions of the ligands around the Mn^{2+} ion to form intra-molecular hydrogen bonds (1:1 complexes in Figure S2) or the dissociation of one or two water molecules to give distorted structures with the Mn^{2+} ion four- or five-coordinated (1:2 complexes in Figure S2). This difficulty in optimizing Mn^{2+} octahedral complexes with O-donor ligands was previously observed [33]. In addition, other authors [34] argued that Mn^{2+} species have very small energy differences between octahedral and other geometries (*e.g.* trigonal prismatic or tetrahedral) and the coordination in solution is strongly dependent on the nature of the ligands (monodentate/chelate, type of coordinating atom, steric hindrance).

Instead, geometry optimizations with an increasing amount of additional explicit water molecules bound through H-bonds to $[Mn(H_2O)_4L]$ and $[Mn(H_2O)_2L_2]^{2-}$ produced final structures with Mn^{2+} in an octahedral arrangement. The minimum number of "extra" water molecules to give octahedral geometries with all the three L ligands resulted to be two for $[Mn(H_2O)_4L]$ and six for $[Mn(H_2O)_2L_2]^{2-}$. In all cases, vibrational analysis was carried out to confirm that stationary were true minima (*i.e.* no imaginary frequencies present).

For the resulting $[Mn(H_2O)_4L \cdot 2H_2O]$ and $[Mn(H_2O)_2L_2 \cdot 6H_2O]^{2-}$ species, the electron density at the Mn-O(L) critical points according to Bader's AIM theory [Bader, R. F. W., Chem. Rev., 1991, 91 (5), 893-928], which are known to be closely related to bonding strength, [Matta, C. F.; Boyd, R. J. The Quantum Theory of Atoms in Molecules: From Solid State to DNA and Drug Design; Wiley, 2007; p. 11; Kumar, P. S. V.; Raghavendra, V.; Subramanian, V. J. Chem. Sci. 2016, 128 (10), 1527–1536] were calculated.

All the calculations were performed with Gaussian 16 [37].

3. Results and discussion

3.1. Protonation constants

Protonation constants of SAL, PAS and Ac-PAS were determined by potentiometric, UV-Vis and fluorescence techniques. The protonation constants potentiometrically determined are reported in Table 1. Each protonation step leads to the change of spectrophotometric properties of the ligands allowing also a systematic investigation on nature of the related formed species using UV-Vis data. The spectra collected at different pH ranges are reported in Figure S1 in ESI for all the investigated ligands and 4-amino benzoic acid.

SAL is characterized by two log K values, the lower attributed to the carboxylic group, and the higher to the phenolic group (Table 1). Figure 1A presents the absorptivity spectra of the differently protonated species of SAL, calculated by HypSpec with the protonation constants in Table 1. The LH_2 species shows two bands with absorptivity maxima at 237 nm and 302 nm, $[LH]^-$ at 231 nm and 296 nm, and $[L]^{2-}$ at 246 nm and 316 nm.

Table 1. Protonation constants (log K) obtained by potentiometry at 25 °C and 0.1 M NaCl ionic strength.

	SAL	PAS	Ac-PAS
-COOH	3.10(1)	2.67(1)	3.29(3)
-NH$_3^+$	-	3.95(2)	-
-OH	13.6(1)	13.5(1)	13.4(1)

PAS has three log K values, due to the presence of amino group (Table 1). The LH_3^+ species shows two bands at 235 nm and 300 nm, LH_2 species three bands at 230 nm, 275 nm and 302 nm, $[LH]^-$ two bands at 262 nm and 300 nm, and $[L]^{2-}$ a shoulder at 262 nm and a band at 310 nm (Figure 1B).

8

Ac-PAS has two log K values. The completely protonated species LH_2 shows two bands at 271 nm and at 307 nm (Figure 1C). The [LH]⁻ species is characterized by two bands at 263 nm and 302 nm, whose intensities decrease during the second deprotonation that gives the $[L]^{2-}$ species characterized by the bands at 263 nm and 318 nm (Figure 1C). The band at ≈260-270 nm can be attributed to presence of –NR (R = H, Ac) group in the para-position. This band, not present in the spectra of SAL, appears in the spectra of 4-aminobenzoic acid (Figure 1D). Moreover, absorptivity spectra of PAS, Ac-PAS and 4-aminobenzoic acid are more intense than that of SAL.

4-aminobenzoic acid has two log K values at acidic pH, one attributed to the carboxylic group, and the second to the amino group. LH_2 species has one band at 285 nm, which becomes more intense after deprotonation (Figure 1D). During the second deprotonation, the spectra are shifted to lower wavelengths and the $[L]^{2-}$ species is characterized by the band at 265 nm (Figure 1D).
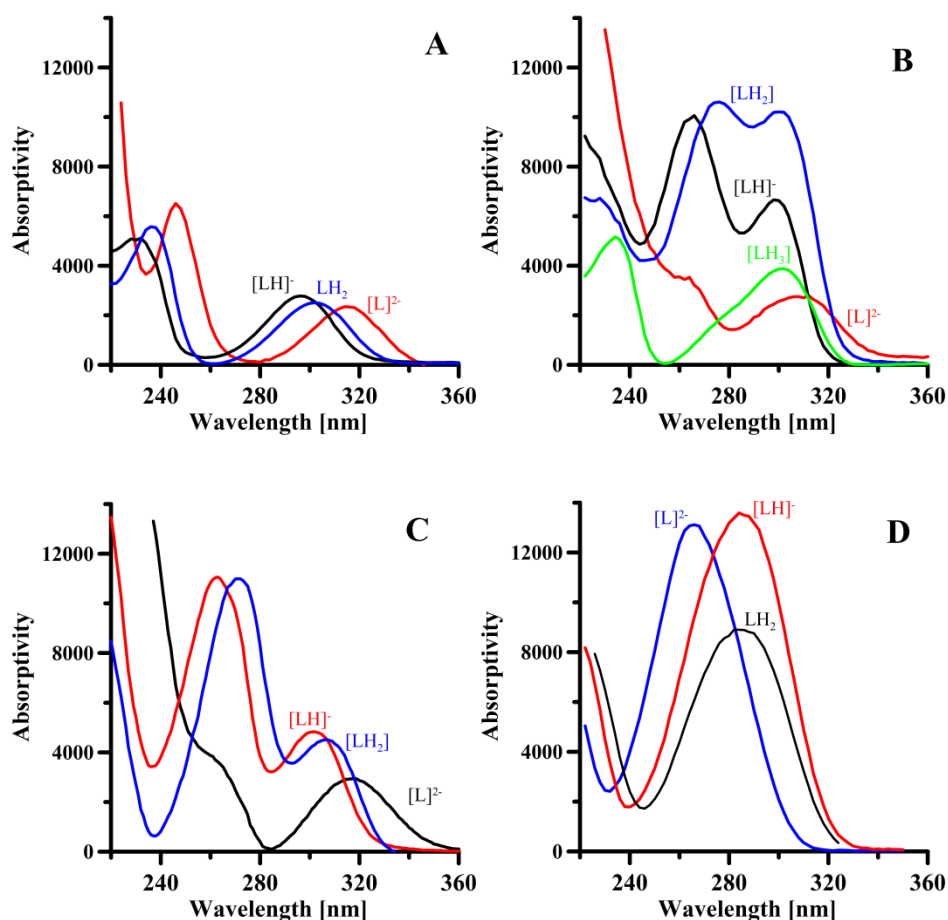

Figure 1. Absorptivity spectra of SAL (A), PAS (B), Ac-PAS (C) and 4-aminobenzoic acid (D) calculated with HypSpec program [19].

Time-dependent DFT calculations have been carried out to check the correspondence between absorption spectra and given species. The minimum energy structures are reported in Figure 2. In all cases, an intramolecular hydrogen bond is formed between the carboxylic group and the hydroxyl moiety. For $PASH_2$, two possible structures have been optimized depending on the protonation of the amine group ($PASH_2$(a) and $PASH_2$(b)).

The calculated spectra for SAL ligand are reported in Figure 3A. The lowest energy excitations involve HOMO – LUMO transitions (MO displayed in Figure S3) and are strongly sensitive to the protonation state of the ligands. For $SALH_2$, the lowest energy excitation corresponds to a band centered at $\lambda_{calc} = $ 276 nm, which is shifted to $\lambda_{calc} = 261$ nm when SALH is formed. For SAL this band is red-shifted to $\lambda_{calc} = 283$ nm. These variations are in qualitative agreement with the experimental spectrum (Figure 1A) even if they systematically underestimate the wavelength at which the band is centered. For $PASH_3$ the lowest energy excitation is at $\lambda_{calc} = 271$ nm. Two possible $PASH_2$ isomers have been considered: one with protonated amine and one with protonated carboxylic acid ($PASH_2$(a) and (b) in Figure 2). Our results show that the $PASH_2$(b) form is energetically favored ($\Delta E = E$ (b) - E(a) = -15.4 kcal mol^{-1} in water) and also the calculated spectra (Figure 3B) is in agreement with the experimental spectrum (λ_{calc} = 271 nm with a shoulder at 253 nm, Figure 1C). In addition, the calculated spectrum of $PASH_2$(a) presents a maximum at $\lambda_{calc} = 294$ nm which is blue-shifted with respect to that of the starting species $PASH_3$ which is not observed in the experiments. Therefore, the absorbing species in solution is $PASH_2$(b).

The trend of the changes in the maxima relative to the PASH and PAS low energy excitations are in agreement with the experimental ones (for PASH $\lambda_{calc} = 262$ nm, for PAS $\lambda_{calc} = 289$ nm). Also in the case of AcPAS, the calculated spectral changes (276 nm → 265 nm → 289 nm, Figure 3C) are in agreement with the experimental spectra.
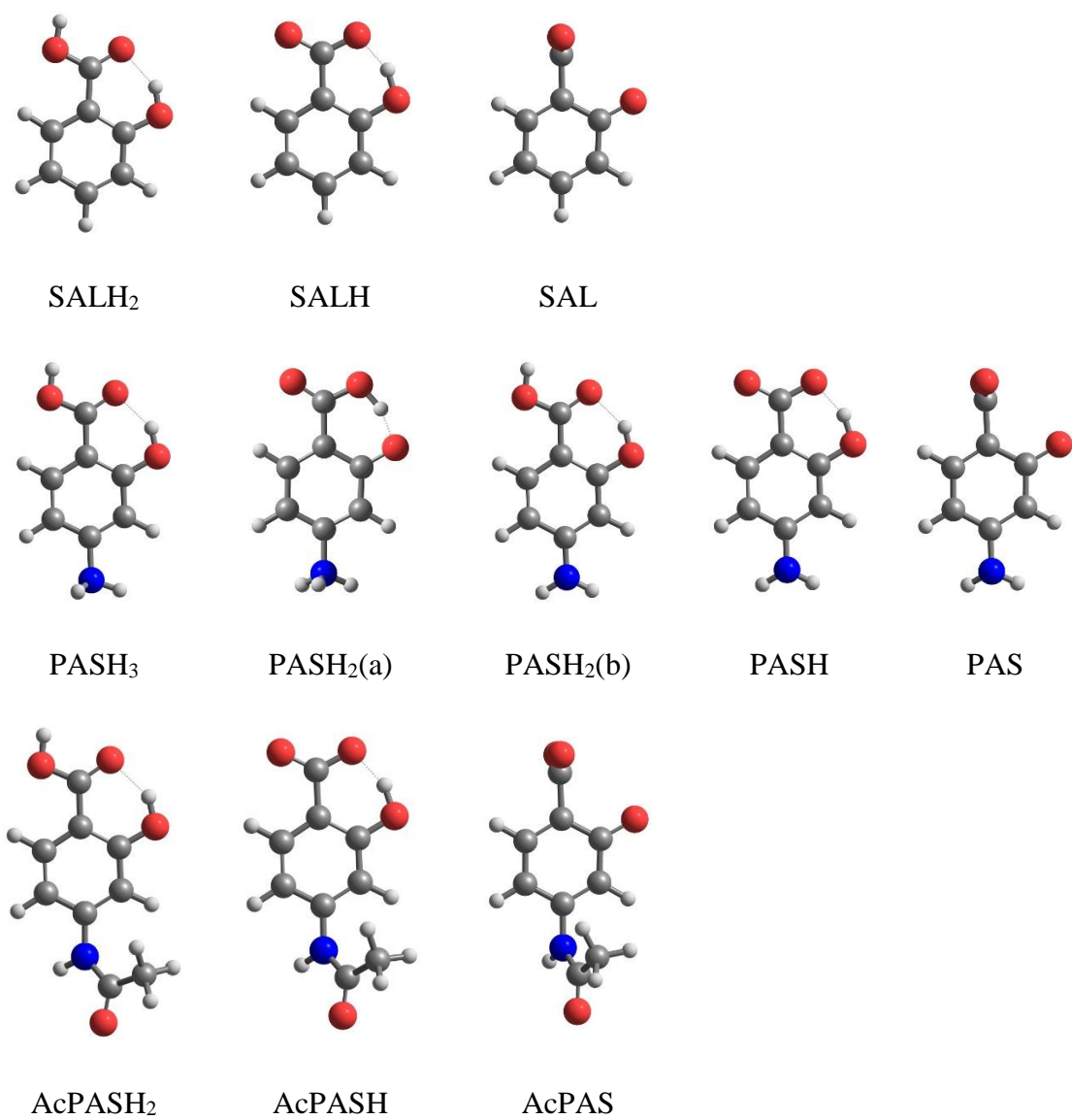
Figure 2. Minimum energy structures of the ligands in their different protonation states.
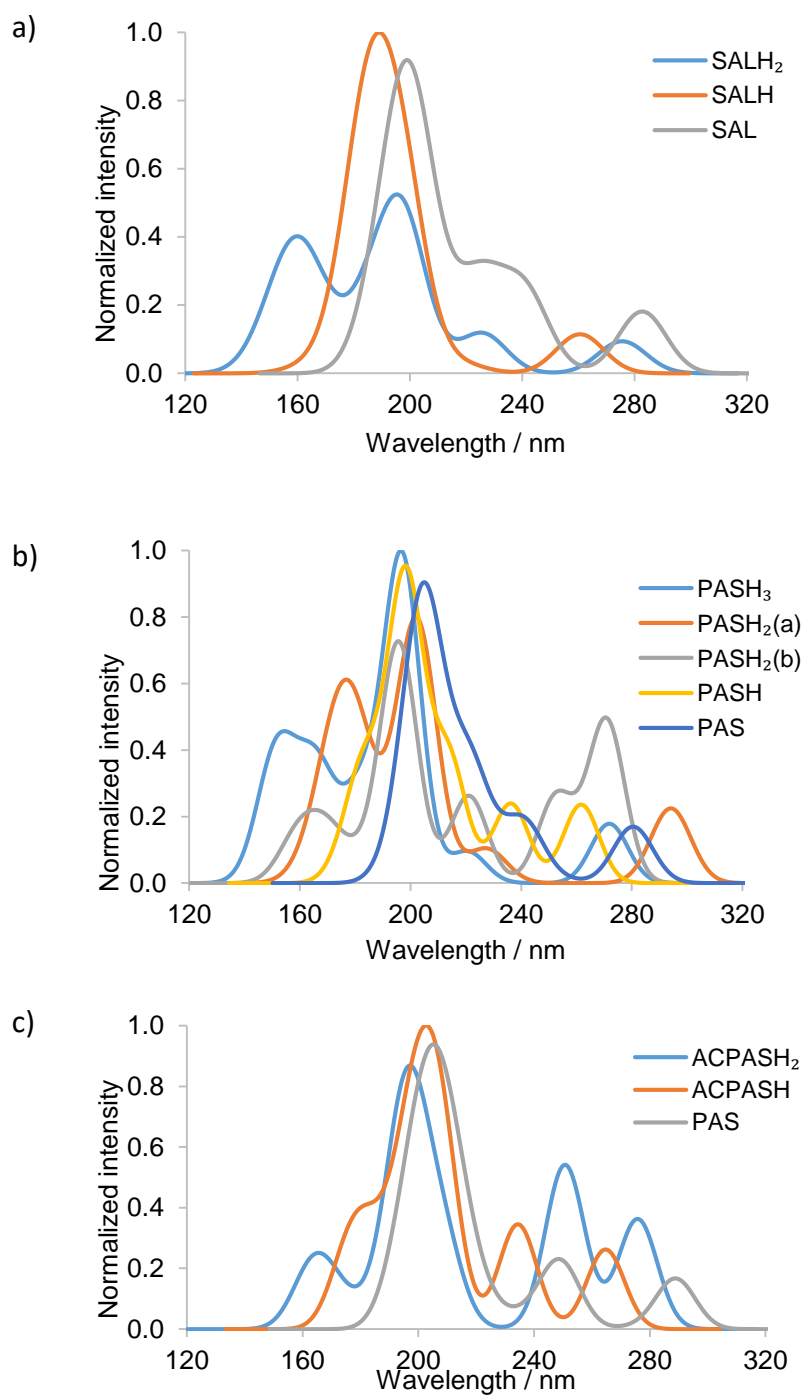
Figure 3. Calculated absorption spectra of the ligands in the 120-320 nm wavelength range. Gaussian broadening applied with half-bandwidth of 16 nm.

The three ligands SAL, PAS and Ac-PAS present fluorescent properties (Figure 4). While fully protonated ligands do not present fluorescence, the remaining species are characterized by fluorescence properties, which change with the protonation degree. SAL has its fluorescence maximum at 409 nm in the monoprotonated form [LH]$^-$; this band shifts at 392 nm and its intensity lowers passing at [L]$^{2-}$ species (Figure 4A and 4B). PAS has its maximum fluorescence at 401nm, when present in the LH$_2$ form. Further deprotonation leads to the lowering of fluorescence intensity and shift to lower wavelengths (392 nm). The last species [L]$^{2-}$ has even lower fluorescence intensity, with the maximum at 392 nm. Ac-PAS presents a minimal fluorescence intensity also in the fully protonated at about 460 nm (Figure 4E and 4F). The first deprotonation leads to a band of marked intensity at 402 nm. The second deprotonation produces relevant ipso- and hypo-chromic effects on this fluorescence band. In the same experimental conditions, Ac-PAS and then SAL (in the [LH]$^-$ form) are the ligands with the most marked fluorescence properties.
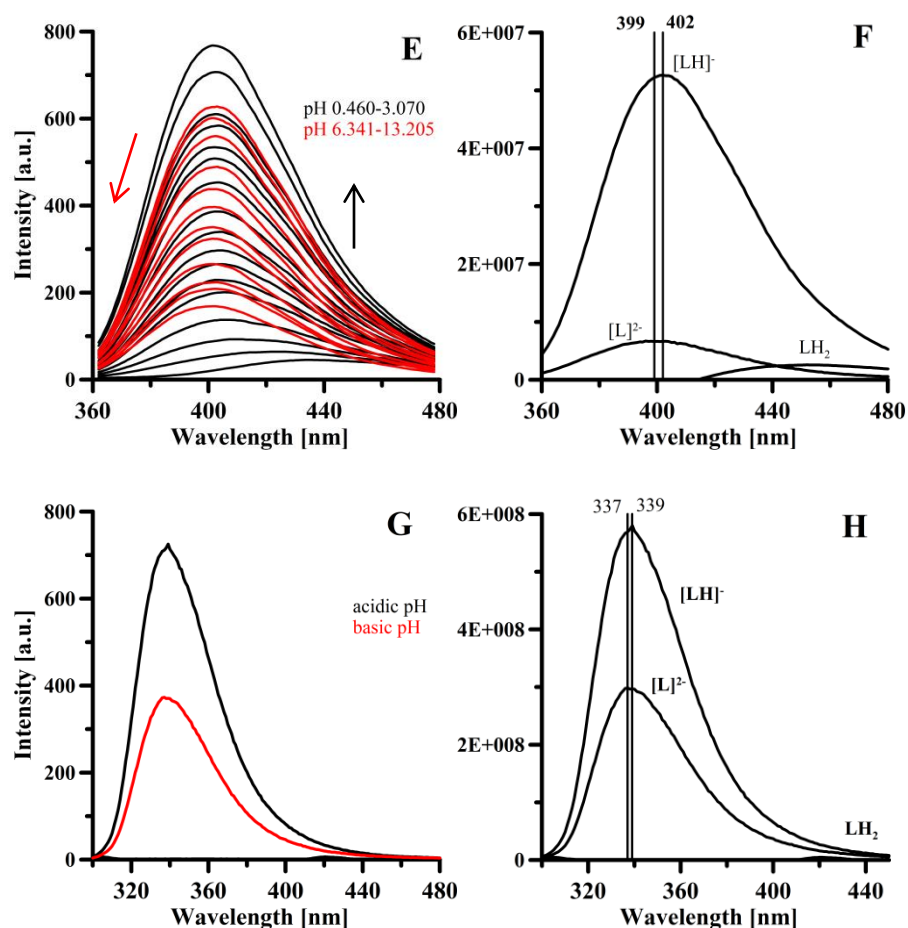

13
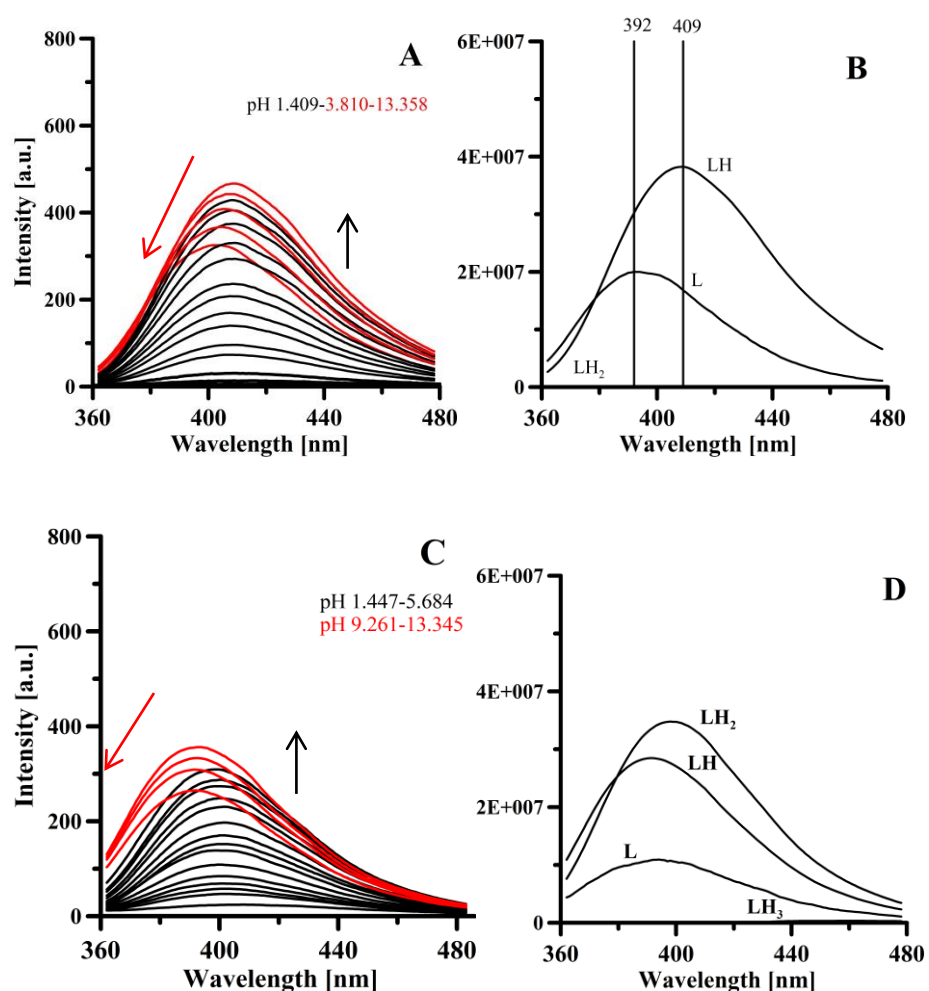
Figure 4. Fluorescence (left) and molar *absorptivity* (right) fluorescence spectra of SAL (A, B), PAS (C, D), Ac-PAS (E, F), 4-aminobenzoic acid (G, H). C[L] = 0.0125 mM, 0.1 M NaCl ionic strength. λ_{Ex} 276 nm, λ_{Em} 286-486 nm.

The increase of fluorescence intensity after the deprotonation of carboxylic group could be reasonably attributed to the formation of a hydrogen bond between $-COO^-$ and $-OH$ groups (Figure 2), as previously suggested [38]. Such intramolecular hydrogen bond leads to the formation of an additional six-membered ring that increases the molecule rigidity. In the same experimental conditions, benzoic acid has no fluorescence properties neither in acidic, nor in basic pH. On the contrary, 4-aminobenzoic acid has fluorescent properties in the $[LH]^-$ and $[L]^{2-}$ forms, significantly shifted to lower wavelengths ($[LH]^-$ species has maximum intensity at 339 nm, and $[L]^{2-}$ species at 337 nm) (Figure 4G and 4H). The absence of $-OH$ group could explain the shift to lower wavelengths. Thus, the log K values obtained by potentiometric titrations of SAL, PAS and Ac-Pas free ligands can be definitely attributed: the most

acidic deprotonation to carboxylic group, while the most basic to the hydroxyl group (Table 1). The speciation plots in Figure 5 show that at physiologic pH 7.4 all ligands are present in the monoprotonated form ([LH]$^-$).
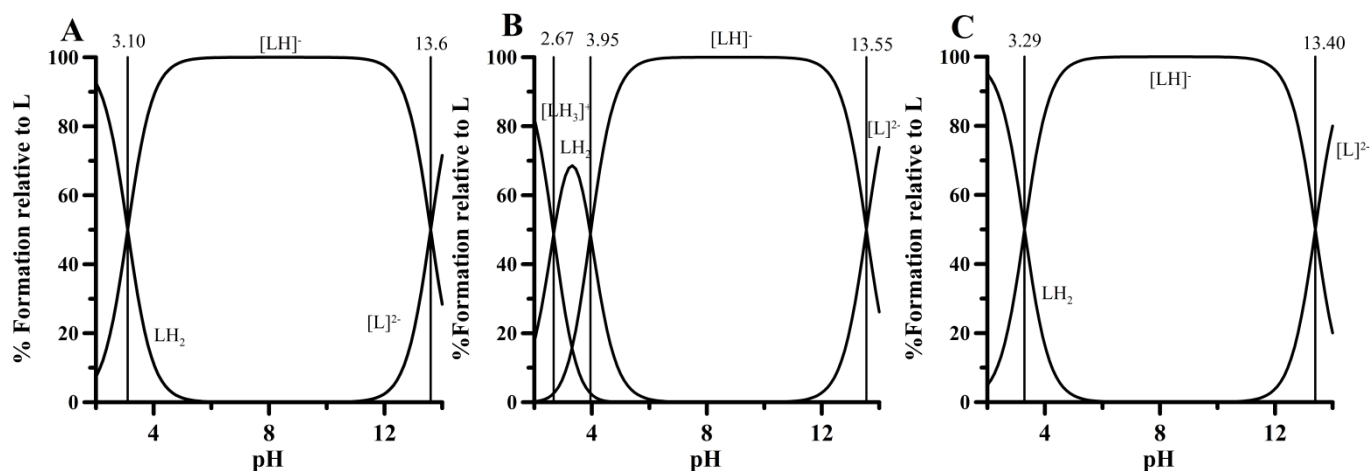

Figure 5. Speciation plots of SAL (A), PAS (B) and Ac-PAS (C) calculated with Hyss program [39] on the base of protonation constants in Table 1.

The presence of strongly electron withdrawing amino group in the aromatic ring in PAS (in para-position) lowers the log K value of carboxylic group (2.67) respect to that of the same group in SAL (3.10). On the contrary, the moderately electron donating amide group in Ac-PAS increases the log K value of carboxylic group (3.29).

3.2. Complex formation with Mn^{2+}

The complex formation equilibria of SAL, PAS and Ac-PAS with the target metal ion Mn^{2+} have been studied by potentiometry and the complex formation constants are reported in Table 2. The related speciation plots show that the MnL complex starts at pH 4, and [MnL$_2$]$^{2-}$ forms above pH 6 with SAL and Ac-PAS, and above pH 9 with PAS (Figures S4).

On the base of the pMn[1] values, the manganese complexes of Ac-PAS are more stable than those with the other two ligands. It has to be remarked the analogous trend of the pK_a value of carboxylic group and the pMn value, which implies a strong involvement of the carboxylic group in Mn^{2+} coordination.

Table 2. Logβ values of manganese complexes at 25°C and 0.1 M NaCl ionic strength. The relative pMn values are also reported.

Species	SAL	PAS	Ac-PAS
[MnL]	10.7(1)	9.9(2)	11.4(2)
[MnL$_2$]$^{2-}$	19.1(2)	17.2(2)	19.8(3)
pMn	6.25	6.02	6.54

EPR spectra were recorded in the systems Mn^{2+}/PAS and Mn^{2+}/Ac-PAS with a molar ratio of 1:5 at a pH value at which MnL complex reach the maximum concentration in aqueous solution (pH 8.6 and 7.1 respectively, see Figure S4). The spectra, reported in Figure 6, are very similar, suggesting the same coordination mode. The hyperfine structure is well evident with the six strong absorptions, corresponding to the $|-1/2, m> \rightarrow |1/2, m>$ 'allowed' transitions ($\Delta M = \pm 1$, $\Delta m = 0$), and in the middle the five pairs of 'forbidden' absorptions ($\Delta M = \pm 1$, $\Delta m = \pm 1$). The anisotropy of x, y and z components is negligible and, at a first approximation, the values of g and A measured can be considered isotropic. The spin Hamiltonian parameters are $g = 2.003$ and $A = 88.8 \times 10^{-4}$ cm^{-1} for PAS and $g = 2.003$ and $A = 88.7 \times 10^{-4}$ cm^{-1} for Ac-PAS. These values are compatible with an octahedral Mn^{2+} species [40-45] and, in particular, with a MnO_6 coordination [46-50]. These parameters are very similar to those of calcite and of the recently characterized Mn^{2+} species formed by ethylvanillin, where Mn^{2+} is surrounded by six oxygen atoms in an octahedral environment [51, 52]. In contrast, A for the aquo-ion $[Mn(H_2O)_6]^{2+}$ ($A \sim 82 \times 10^{-4}$ cm^{-1}) [53, 54] is significantly smaller than that measured for MnL.

---

[1] pM is defined as the negative logarithm of the concentration of free metal ion in solution, when $[M^{n+}]_{tot} = 10^{-6}$ M, $[Ligand]_{tot} = 10^{-5}$ M at pH 7.4.
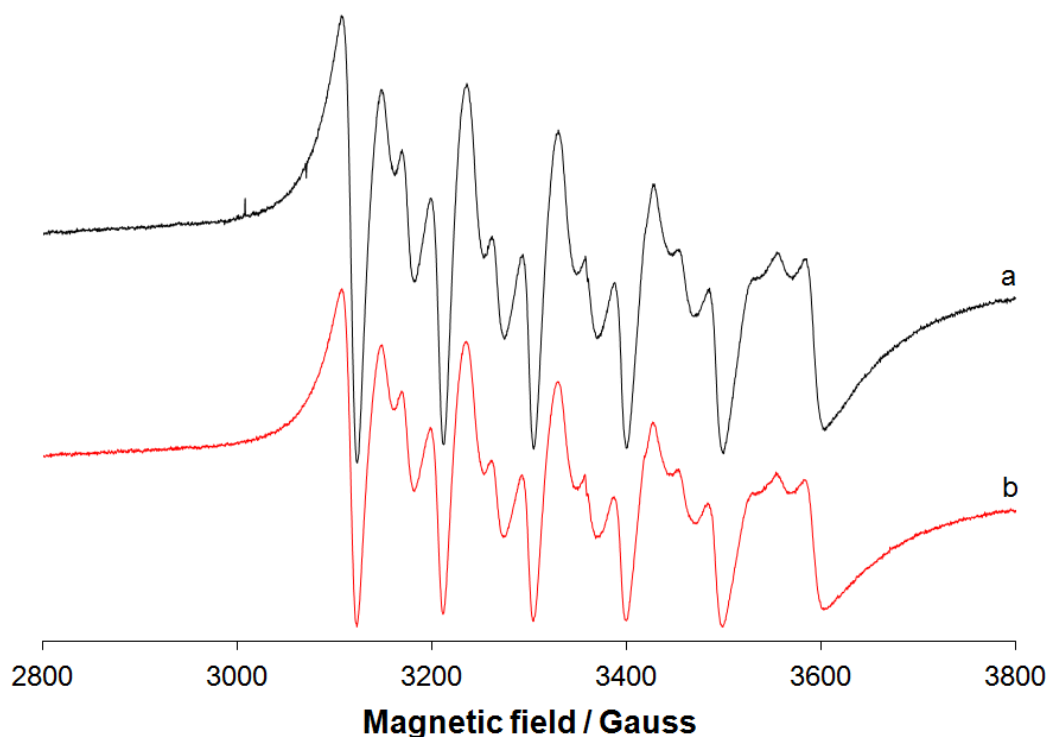
Figure 6. Anisotropic X-band EPR spectra (120 K) of the MnL species formed in the systems containing: (a) Mn^{2+}/Ac-PAS 1:5 (pH 7.1) and (b) Mn^{2+}/PAS 1:5 (pH 8.6).

EPR spectra of the system Mn^{2+}/PAS 1:5 at several pH are shown in Figure 7. It can be observed that, in agreement with the speciation plots in Figure S4, EPR spectroscopy suggests the presence of only one species in aqueous solution in the pH range 7-10, [MnL] ($g = 2.003$ and $A = 88.8 \times 10^{-4}$ cm^{-1}). At pH higher than 10 the spectral signal changes significantly indicating a variation in the Mn^{2+} chemical environment and the formation of a new species, $[MnL_2]^{2-}$. The approximated spin Hamiltonian parameters for this complex are $g \sim 2.00$ and $A \sim 86 \times 10^{-4}$ cm^{-1}.
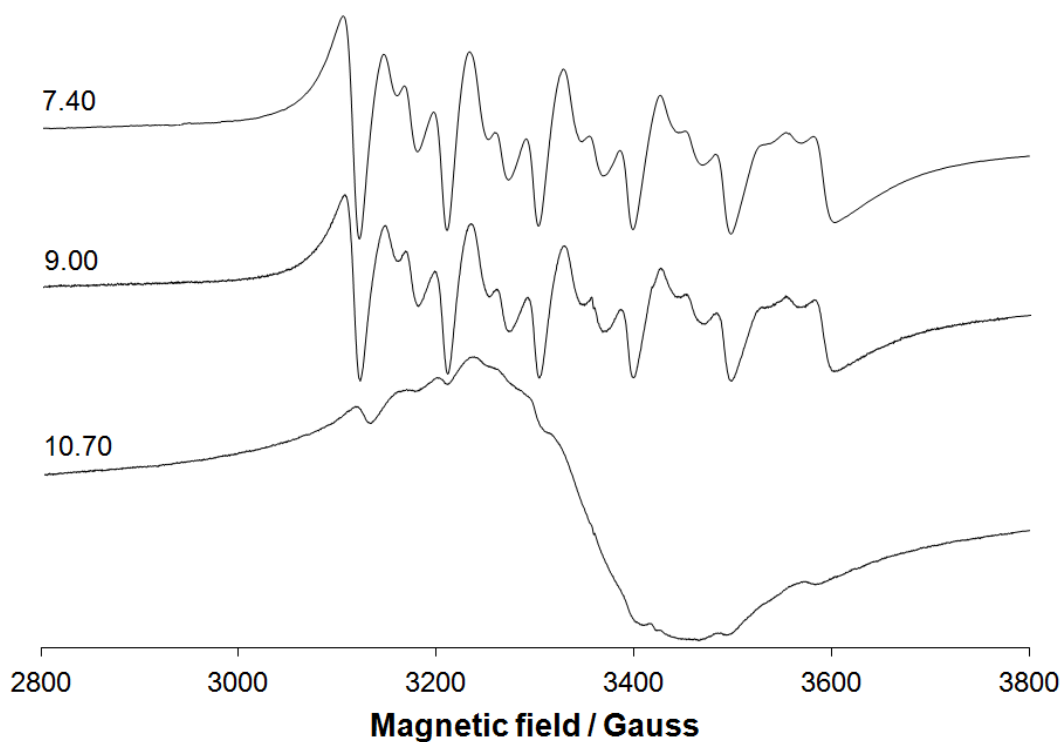
Figure 7. Anisotropic X-band EPR spectra (120 K) recorded on the system Mn^{2+}/PAS 1:5 as a function of pH (Mn concentration was 0.5 mM).

As reported in the Computational details, octahedral geometries in agreement with EPR results were obtained for the Mn^{2+} complexes when second-sphere solvating water molecules were added. This result suggests that water is weakly coordinated to the metal in these species. The minimum energy structures of the $[Mn(H_2O)_4L\cdot 2H_2O]$ and $[Mn(H_2O)_2L_2\cdot 6H_2O]^{2-}$ complexes are shown in Figure 8.
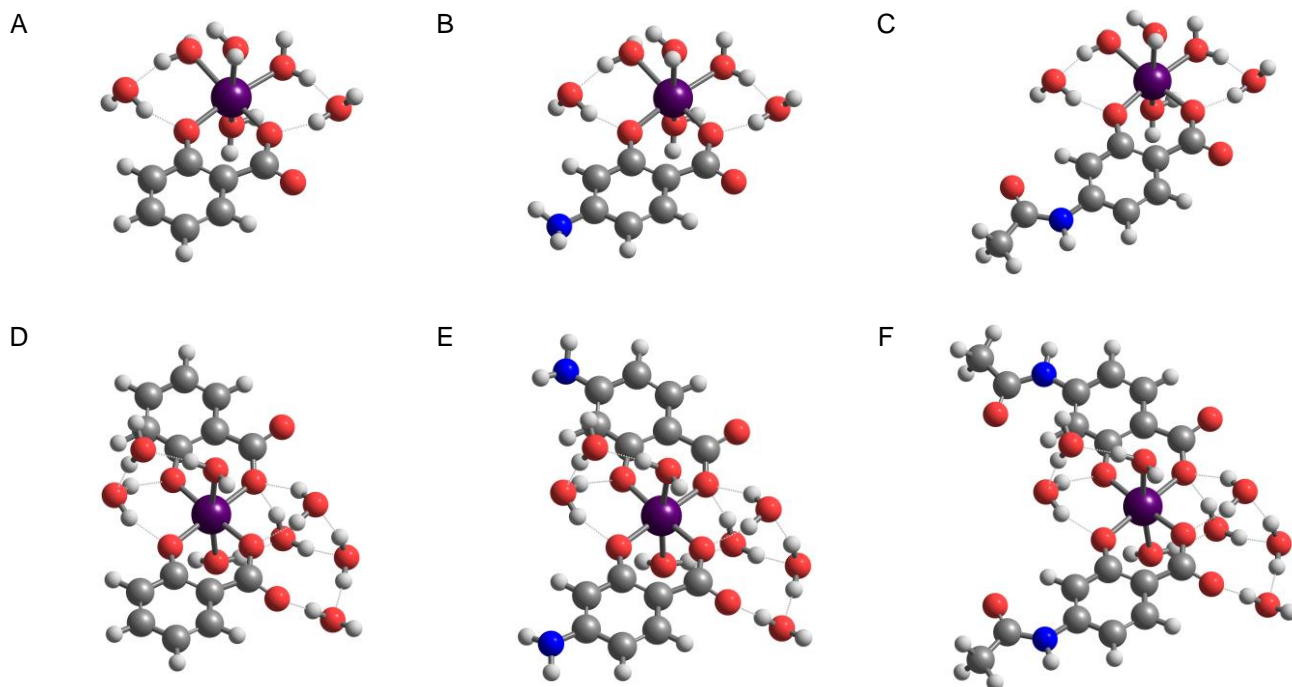
Figure 8. Minimum energy structures calculated at the B3LYP/6-31+G(d,p)/SDD level of theory in CPCM water: A) $[Mn(H_2O)_4(SAL)\cdot 2H_2O]$, B) $[Mn(H_2O)_4(PAS)\cdot 2H_2O]$, C) $[Mn(H_2O)_4(AcPAS)\cdot 2H_2O]$, D) $[Mn(H_2O)_2(SAL)_2\cdot 6H_2O]^{2-}$, G) $[Mn(H_2O)_2(PAS)_2\cdot 6H_2O]^{2-}$, F) $[Mn(H_2O)_2(AcPAS)_2\cdot 6H_2O]^{2-}$.

The two extra water molecules in the MnL species interact with the oxygen atoms of the L ligands in the equatorial plane by means of H-bonds (Figure 8 A-C), while for $[MnL_2]^{2-}$ the six extra water molecules interact both with the oxygen atoms of the L ligands and with the two apical water molecules coordinated to the metal.

The obtained Mn-O(L) bond distances of the optimized MnL and $[MnL_2]^{2-}$ species and the mean absolute error (MAE) on the O-Mn-O angles with respect to an ideal octahedron are reported in Table 3. The calculated MAE standing between 7.5° and 7.2° for the MnL species shows that the optimized structures are distorted octahedral, while the $[MnL_2]^{2-}$ have more regular structures.

The resulting average Mn-O(L) bond distances (Table 3) show that the Mn-O(O$^-$) bonds are systematically shorter than the Mn-O(COO$^-$) ones, although no significant differences in the average bond distance was detected by changing the L ligands.

Table 3. Structural parameters for the MnL and $[MnL_2]^{2-}$ complexes calculated at the B3LYP/6-31+G(d,p)/SDD level in CPCM water.

Species	$r_{Mn-O(COO-)}$ (Å)[a]	$r_{Mn-O(O-)}$ (Å)[b]	Average $r_{Mn-O(L)}$ (Å)[c]	MAE (°)[d]
$[Mn(H_2O)_4(SAL)\cdot 2H_2O]$	2.088	2.068	2.078	7.5
$[Mn(H_2O)_4(PAS)\cdot 2H_2O]$	2.083	2.066	2.074	7.7
$[Mn(H_2O)_4(AcPAS)\cdot 2H_2O]$	2.087	2.071	2.081	7.6
$[Mn(H_2O)_2(SAL)_2\cdot 6H_2O]^{2-}$	2.167	2.110	2.138	2.6
$[Mn(H_2O)_2(PAS)_2\cdot 6H_2O]^{2-}$	2.163	2.110	2.136	2.5
$[Mn(H_2O)_2(AcPAS)_2\cdot 6H_2O]^{2-}$	2.166	2.111	2.138	2.5

Calculated bond distances for the [a]Mn-O(COO⁻) and [b]Mn-O(O⁻) bonds (average of the two bonds per type for $[MnL_2]^{2-}$) and average Mn-O(L) bond distance with the L ligands (L = SAL, PAS, AcPAS). [d]Mean Absolute Error calculated as $\frac{\sum_i^n |\alpha_i - 90|}{n}$ on n O-Mn-O α angles formed by Mn with the L ligands and the water molecules.

The calculated values of the electron density at the Mn-O(COO⁻) and Mn-O(O⁻) critical points according to the AIM theory [Bader, R. F. W., Chem. Rev., 1991, 91 (5), 893-928] are reported in Table 4.

Table 4. AIM electron density at the Mn-O(L) critical points for the MnL and $[MnL_2]^{2-}$ species.

Complex	$\rho_{Mn-O(COO-)}$[a]	$\rho_{Mn-O(O-)}$[b]	Average $\rho_{Mn-O(L)}$[c]
$[Mn(H_2O)_4(SAL)\cdot 2H_2O]$	0.063	0.067	0.065
$[Mn(H_2O)_4(PAS)\cdot 2H_2O]$	0.064	0.068	0.066
$[Mn(H_2O)_4(AcPAS)\cdot 2H_2O]$	0.063	0.067	0.065
$[Mn(H_2O)_2(SAL)_2\cdot 6H_2O]^{2-}$	0.052	0.060	0.056
$[Mn(H_2O)_2(PAS)_2\cdot 6H_2O]^{2-}$	0.052	0.060	0.056
$[Mn(H_2O)_2(AcPAS)_2\cdot 6H_2O]^{2-}$	0.052	0.060	0.056

AIM electron density calculated at the [a]Mn-O(COO⁻) and [b]Mn-O(O⁻) bond critical points (average of the two bonds per type for $[MnL_2]^{2-}$) and [c]average value of all the Mn-O(L) bonds with the L ligands (L = SAL, PAS, AcPAS).

As can be seen from the reported data, a slight greater electron density for the Mn-O(O⁻) bonds in comparison with the Mn-O(COO⁻) ones is detectable at least for the $[MnL_2]^{2-}$ complexes. This could indicate a stronger Mn-O(O⁻) bond with respect to Mn-O(COO⁻), which can be related to the shorter Mn-O(O⁻) bond lengths reported in Table 3. However, no difference in the electron densities, and thus in the bond strength, is observed by changing the L ligand. This result could be caused by the poor differences

between SAL, PAS and AcPAS in terms of coordination properties, given that they are different only for the substituent in *orto* and *para* positions with respect to the two coordinating moieties. This suggests that the logβ values reported in Table 2, which show that the formation of the Mn-L complexes is more favorable following the AcPAS > SAL > PAS order, could not primarily influenced by the strength of the Mn-L interaction. Evidently this difference in stability could be due to a delicate balance of metal-ligand interaction and solvation properties of the reagents and products as previously observed [55-57]. To investigate the formation of the MnL and $[MnL_2]^{2-}$ complexes and check the dependence of the obtained results upon the employed level of theory, Gibbs free energies for the reactions have been calculated (Table 5):
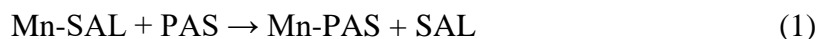
$$Mn\text{-}SAL + PAS \rightarrow Mn\text{-}PAS + SAL \qquad\qquad (1)$$
$$Mn\text{-}SAL + AcPAS \rightarrow Mn\text{-}AcPAS + SAL \qquad\qquad (2)$$

Table 5. Reaction free energies for the reactions (1) and (2) calculated at different levels of theory.

Functional	Basis set	Solvation model	ΔG (kcal mol^{-1})			
			Mn-SAL + PAS → Mn-PAS + SAL*		Mn-SAL + AcPAS → Mn-AcPAS + SAL*	
			[MnL]	$[MnL_2]^{2-}$	[MnL]	$[MnL_2]^{2-}$
B3LYP	6-31+G(d,p)/SDD	CPCM	-2.2	-3.6	2.2	4.5
		SMD#	-0.4	-4.0	3.6	6.6
	6-31+G(d,p)	CPCM	-2.9	-6.3	-1.0	-1.3
		SMD#	-2.3	-1.3	1.0	0.6
	6-311+G(d,p) †	CPCM	-2.9	-5.1	-0.3	-0.4
		SMD#	-2.8	-1.2	-1.0	2.5
	aug-cc-pvTZ†	CPCM	-3.1	-5.3	-0.3	-0.4
M06	6-31+G(d,p)	CPCM	-3.0	-6.5	-3.5	-2.1

*For $[MnL_2]^{2-}$ complexes, the reactions taken into account are Mn-SAL$_2$ + 2PAS → Mn-PAS$_2$ + 2SAL and Mn-SAL$_2$ + 2AcPAS → Mn-AcPAS$_2$ + 2SAL.

energy calculations using the SMD solvation for the minimum energy structures obtained with CPCM.

†energy calculations with the B3LYP 6-31+G(d,p)/SDD geometries.

As can be seen from Table 5, the substitution of the SAL by PAS results always favorable (negative ΔG) with the B3LYP functional, indifferently from the employed basis set or solvation model applied. The substitution of SAL by AcPAS is always less favorable than that with PAS. On the basis of such

theoretical results the predicted stability of the MnL and $[MnL_2]^{2-}$ complexes follows the order PAS > SAL > AcPAS or PAS > AcPAS > SAL. This is different from the experimental logβ values which show the AcPAS > SAL > PAS stability order. On the other hand, the results obtained with the M06 functional show that the substitution of SAL by AcPAS is slightly more favorable than the substitution by PAS, thus producing the trend AcPAS > PAS > SAL for the 1:1 complexes, which is closer to the experimental. These results show that the calculated free energies strongly depend upon the employed functional, with the M06 providing the most accurate results. On the other hand, no significant variations are showed by changing the basis set or the solvation model. A similar dependence of parameters such as dissociation energies and affinity with ligands from the level of theory, especially for manganese complexes, has been already observed by other authors. [N. Russo, E. Sicilia, M. Toscano, A. Grand, International Journal of Quantum Chemistry, Vol. 90, 903–909 (2002); M. Lundberg, P. E. M. Siegbahn, Comput Chem 26: 661–667, 2005; X. Xu, D. Truhlar, J. Chem. Theory Comput. 2012, 8, 80–90] In conclusion the computational results are able to reproduce only partially the experimental stability order. This discrepancy could be due to the incomplete inclusion of the solvation effects: in our models the solvation is introduced as continuum and with explicit water molecule placed around the metal ion, while the ligand is not completely solvated.

3.3 Complexation with Cu^{2+} and Fe^{3+} ions

The complex formation equilibria of SAL, PAS and Ac-PAS with the essential metal ions Fe^{3+} and Cu^{2+} have been studied by potentiometric methods (in the case of Fe^{3+}, by a joined potentiometric-spectrophotometric method) and the related overall stability constants are reported in Table 6. Cu^{2+} ion forms complexes with SAL, PAS and Ac-PAS more stable than those of manganese. SAL forms the most stable species and the formation of CuL starts at pH 2.5 (Figure S5, speciation plots of Cu^{2+} complexes). Such complex hydrolyzes above pH 5 giving the $[CuLH_{-2}]^{2-}$ species, which precipitates at pH > 7. PAS forms from pH 5 only a $[CuL_2]^{2-}$ complex with low water solubility that precipitates at physiological pH while Ac-PAS forms only a $[CuL_2]^{2-}$ complex that hydrolyzes from pH 5.5 giving a $[CuLH_{-2}]^{2-}$ species of low solubility, which precipitates at physiological pH (Figure S5).

Table 6. Logβ values of Cu^{2+} and Fe^{3+} complexes at 25°C and 0.1 M NaCl ionic strength. The relative pCu and pFe values are also reported.

Species	SAL	PAS	Ac-PAS
[CuL]	12.6(4)	-	-
[CuL$_2$]$^{2-}$	-	22.4(6)	22.8(6)
[CuLH$_{-2}$]$^{2-}$	1.6(4)	-	16.4(2)
pCu	7.98	6.30	7.65
[FeL]$^+$	16.10(9)	19.06(8)	15.97(1)
[FeLH$_{-2}$]$^{3-}$	-2.8(1)	-	1.03(5)
[FeLH$_{-4}$]$^{3-}$	-	-	-6.20(8)
[FeL$_2$]-	30.58(5)	32.44(7)	30.68(7)
[FeL$_2$H$_{-2}$]$^{3-}$	20.77(6)	20.6(1)	23.12(7)
[FeL$_3$]$^{3-}$	43.02(8)	44.0(1)	44.89(4)
pFe	15.01	16.33	17.42

The complexation of Cu^{2+} ion with PAS at molar ratio 1/5 was studied by EPR in aqueous solution as a function of pH. The results are shown in Figure 9. After aquo-ion (indicated with **Cu^{2+}**), a minor species is observed in the pH range 3.5-4.5 (indicated with **I**) characterized by $g_z \sim 2.38$ and $A_z \sim 134 \times 10^{-4}$ cm^{-1}. This species is the mono-chelated complex, revealed by potentiometry in the systems with Mn^{2+} and Fe^{3+} and the low concentration in solution – suggested by EPR spectroscopy – could be the reason that precludes its detection with Cu^{2+}. At pH higher than 5.0, only one species is detected in solution with $g_z = 2.329$ and $A_z = 169.4 \times 10^{-4}$ cm^{-1} (**II** in Figure 9); these parameters are consistent with a CuO_4 equatorial coordination and the formation of [CuL$_2$]$^{2-}$ [58]. The order of the g values, $g_z \gg g_y \sim g_y > 2.0023$ indicates a ground state based on the Cu-$d_{x^2-y^2}$ orbital and a geometry with tetragonal symmetry such as an elongated octahedron [59, 60]. At pH > 8 the spectra change further and another species is revealed (**III** in Figure 9); its spin Hamiltonian parameters are $g_z = 2.302$ and $A_z = 178.0 \times 10^{-4}$ cm^{-1} and could suggest for this system the existence of [CuLH$_{-2}$]$^{2-}$ in aqueous solution, as potentiometry indicates

for SAL and Ac-PAS. At strongly basic solution the last ligand coordinated to the metal ion in the form L^{2-} is replaced by two OH^- ions with the formation of the hydroxide complex $[Cu(OH)_4]^{2-}$.
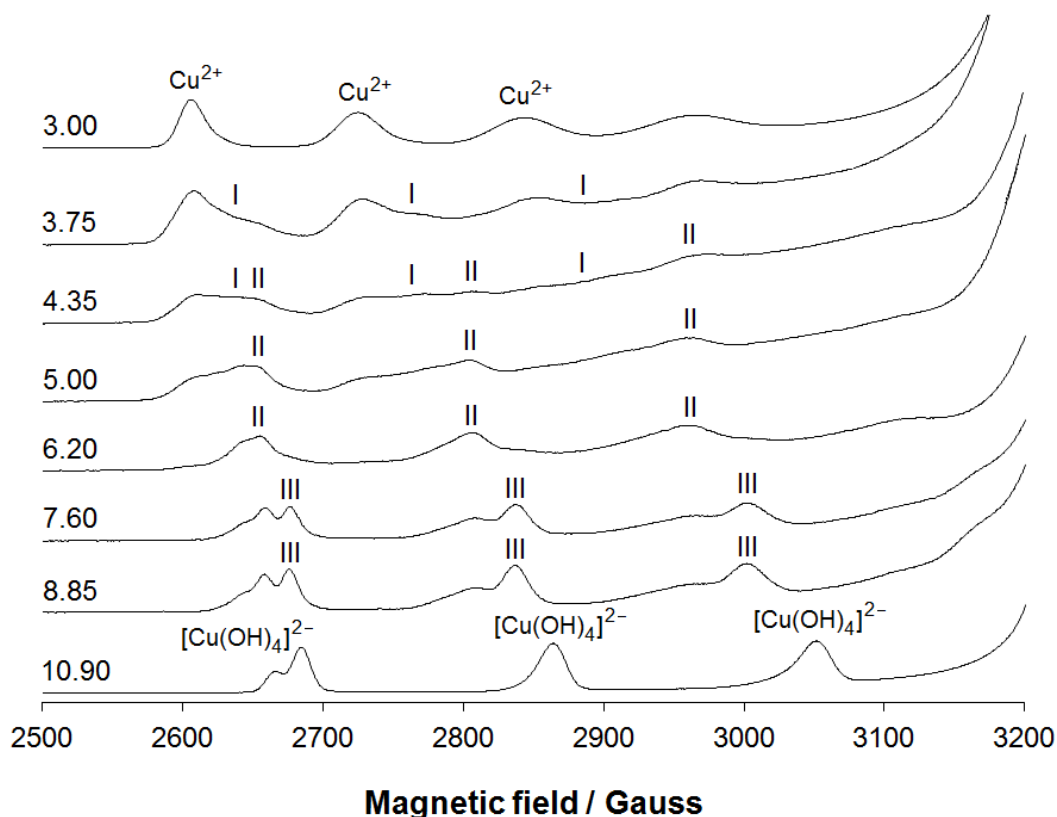

Figure 7. Anisotropic X-band EPR spectra (120 K) recorded on the system Cu^{2+}/PAS 1/5 as a function of pH (Cu concentration was 0.5 mM). With **I**, **II** and **III** the species [CuL], $[CuL_2]^{2-}$ and $[CuLH_{-2}]^{2-}$ are indicated, while Cu^{2+} and $[Cu(OH)_4]^{2-}$ denote the aquo-ion and tetrahydroxidecuprate(II).

The red colored complexes with Fe^{3+} ions are already formed at very acidic pH and therefore the stabilities of $[FeL]^+$ complex was determined only spectrophotometrically (Figure 10). In the range pH 0-3, all the studied ligands form iron complexes with bands at 524 nm, 500nm and 520 nm for SAL, PAS and Ac-PAS respectively (Figure 10). At higher pH (3-5), the bands are shifted to lower wavelengths (Figure 11) due to the significant formation of 1:2 and 1:3 complexes. Clear isosbestic points are observed at 492 nm, 485 nm and 520 nm for SAL, PAS and Ac-PAS relative to the presence of the equilibrium between the $[FeL_2]^-$ and $[FeL_3]^{3-}$ species.
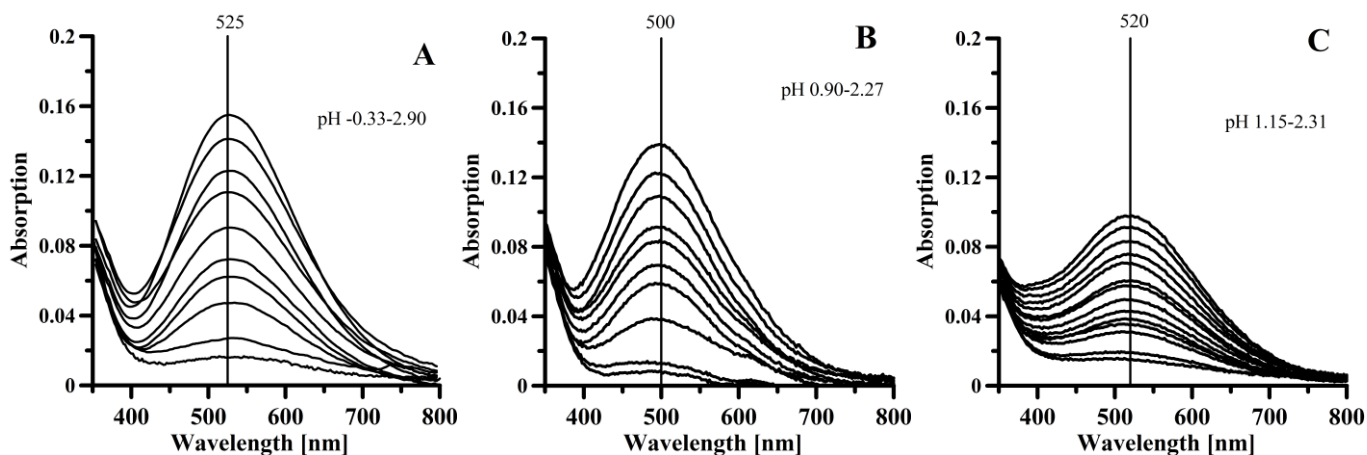
Figure 8. Vis spectra of iron complexes with SAL (A), PAS (B) and Ac-PAS (C) in strongly acidic pH. Ligand concentrations were 0.5 mM and a 1:5 metal to ligand ratio was used, 0.1 M NaCl ionic strength and optical pathway 1 cm.

The $[FeL]^+$, $[FeL_2]^-$ and $[FeL_3]^{3-}$ complexes present characteristic absorptivity bands (Figure 12), which allow to reliably determine the stability constants of the formed complexes from the joined potentiometric-spectrophotometric titrations.

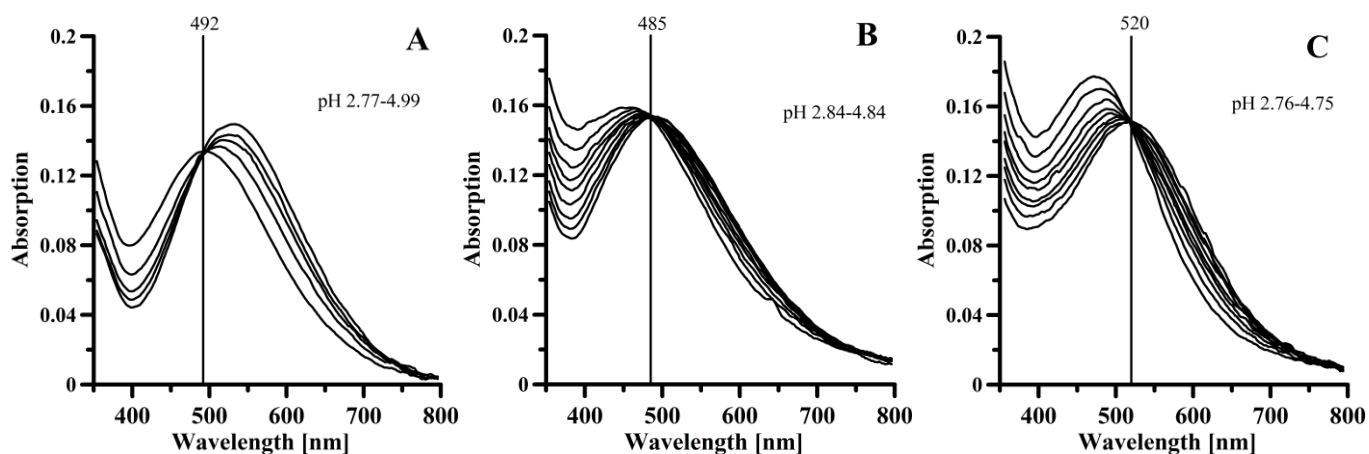**Figure 9.** Visible spectra of iron complexes with SAL (A), PAS (B) and Ac-PAS (C) in the pH range about pH 2.7-5. Ligand concentration was 0.5 mM and a 1:5 metal to ligand ratio, 0.1 M NaCl ionic strength and optical path length 1 cm were used.
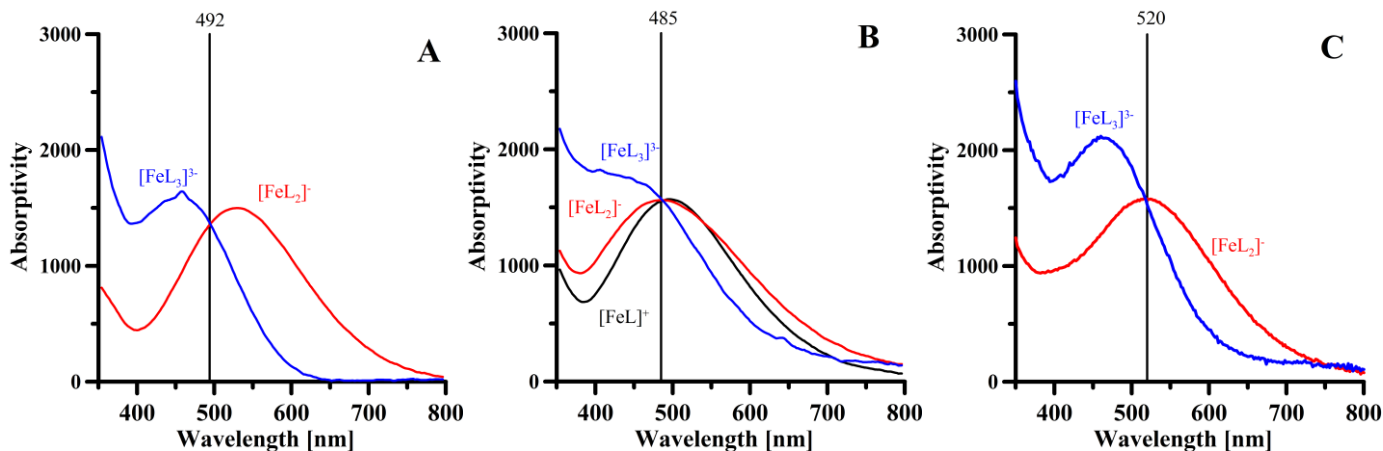
Figure 10. Absorptivity spectra of iron complexes with SAL (A), PAS (B) and Ac-PAS (C) calculates with HypSpec program.

The obtained results are presented in Table 7, and the related speciation plots in Figure S6. The summary of results indicates that SAL forms $[FeL]^+$ complex from pH 1, which transforms into $[FeL_2]^-$ complex above pH 2, and then, above pH 3, into $[FeL_3]^{3-}$ species. Such complex is not stable at physiologic pH and hydrolyzes into $[FeL_2H_{-2}]^{3-}$ complexes. At pH >8 only $[FeLH_{-4}]$ complexes are present.

PAS forms Fe^{3+} complexes more stable than those of SAL (Table 7). $[FeL]^+$, $[FeL_2]^-$ and $[FeL_3]^{3-}$ complexes are formed from pH 1, 3 and 4 respectively. Again, PAS $[FeL_3]^{3-}$ complex hydrolyzes at physiological pH.

Ac-PAS forms the most stable Fe^{3+} complex. At the acidic pH 1-4 $[FeL]^+$, $[FeL_2]^-$ and $[FeL_3]^{3-}$ complexes are formed, which also hydrolyze at physiological pH such complexes. Over pH 8, only $[FeLH_{-4}]^{3-}$ are present in the solution.

3.4 Speciation studies

An evaluation of the scavenge action of PAS and AcPAS toward Mn^{2+} based on the thermodynamic results of the complexation equilibria of these two ligands (Table 2) is presented. In the actual case, the metabolism of PAS leads to a derivative with unusual stronger chelating ability than the parent molecule. In order to perform a speciation study, besides the knowledge of protonation and Mn^{2+} complex formation constants, we need an estimation of Mn^{2+}, PAS and AcPAS concentrations in the organism.

The concentrations of PAS and of its metabolite in plasma can be coarsely evaluated from the pharmacokinetic plot reported by Hong et al. in 2011 [12]: the entire dose intravenously administered is found in plasma at time zero, it is halved in about 40' and is practically reduced to zero in five hours. The concentration of AcPAS reaches a maximum in about 90' with a value about 1/8 of the initial concentration of PAS, and goes to zero at the same time of the parent molecule. The concentrations in the brain are about 100 times lower than the initial one in plasma when expressed in mg/g of tissue, but should be supposed higher in plasma circulating in the brain. The brain concentration of AcPAS is almost double than that of PAS, and assumes characteristic values in the different regions. Therefore, in our simulation we assumed a set of concentrations of PAS ranging from the total injected PAS diluted in five liters of circulating plasma to 1/100 up to 1/1000 of this concentration. In the meantime different ratios AcPAS/PAS were assumed, from zero to two. The evaluation of Mn^{2+} presents some greater difficulties. Two rough limit values of the total amount of toxic metal ion in the organism can be assumed:

- the lower, the daily amount [9-10] excreted in urines (disregarding the possible fecal excretion),
- the higher, up to 60 times this value (15 weeks x four days) x daily excretion , considering that the 3.5 months treatment was able to remove all the metal ion contained in the body, and no further Mn poisoning occurred during the treatment.

Table 11. Total molar concentrations of PAS (first column), of AcPAS and of Mn^{2+} (last column) combined in the speciation plots (Figure 13).

[AcPAS]/[PAS]	0	0.1	0.5	1.0	2.0	
[PAS] mol L^{-1}			[AcPAS] mol L^{-1}			[Mn^{2+}] mol L^{-1}
7×10^{-3}	0	7×10^{-4}	3.5×10^{-3}	7×10^{-3}	1.4×10^{-2}	2.4×10^{-8}
7×10^{-4}	0	7×10^{-5}	3.5×10^{-4}	7×10^{-4}	1.4×10^{-3}	0.1×10^{-6}
7×10^{-5}	0	7×10^{-6}	3.5×10^{-5}	7×10^{-5}	1.4×10^{-4}	0.5×10^{-6}
7×10^{-6}	0	7×10^{-7}	3.5×10^{-6}	7×10^{-6}	1.4×10^{-5}	1.4×10^{-6}

Using a number of the possible combinations among the above limiting values (Table 8) we performed speciation calculations using the program Hyss [39], and the results are presented in Figure 13. The percent of Mn^{2+} in the various form with respect to the assumed total concentration are reported, and the daily excreted amount, expressed in mg/24 h.

Even though the rough simplifying assumptions, the whole of these data allows some confident considerations: PAS in absence of its metabolite ([AcPAS]/[PAS] = 0 in the figures) is able to bind Mn^{2+} ions by forming the 1:1 complex, the percent of complexed manganese decreasing with the PAS concentration.
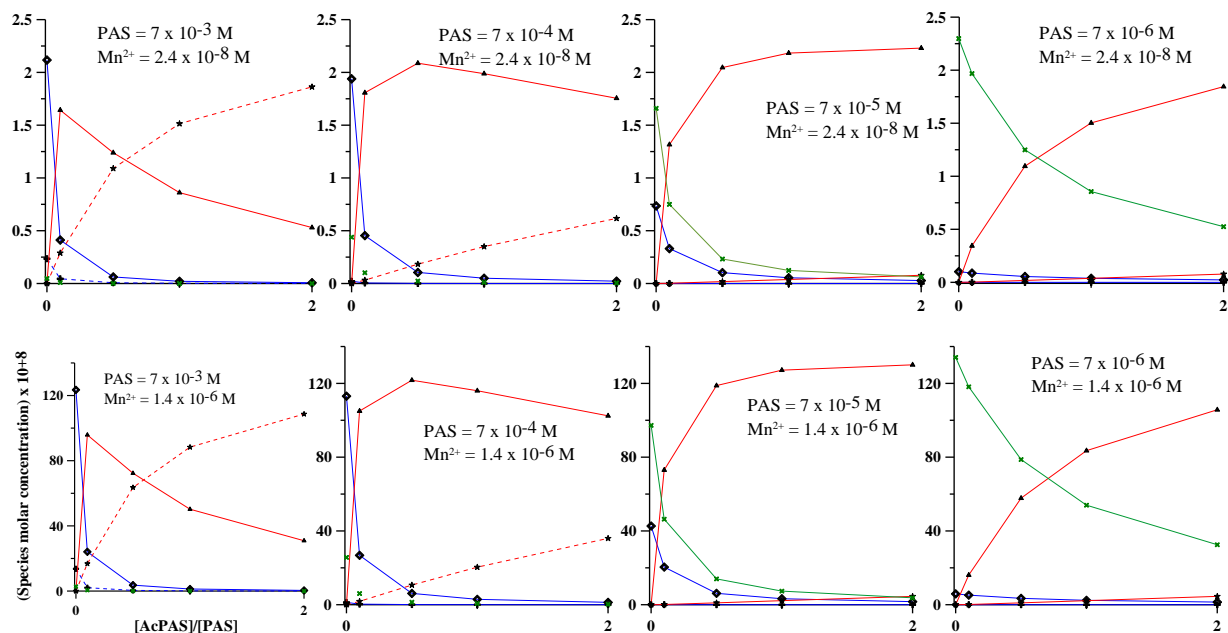

Figure 12. Molar concentrations of the different complexes of Mn^{2+} with PAS (1:1 complex as blue line) and AcPAS(1:1 complex as red continuous line, 1:2 complex as red dashed line), multiplied by 10^8. The upper figures are related to a total Mn^{2+} concentration 0.024×10^{-6} M (a total body burden of Mn^{2+} of 7.2 µg); the lower figures are related to a total Mn^{2+} concentration 1.4×10^{-6} M (a total body burden of Mn^{2+} of 384.6 µg).

The figures on the left are not realistic when the ratio [AcPAS]/[PAS] becomes > 0.1 since the concentration of PAS should decrease with the formation of its metabolite; nevertheless they show that a 10% of AcPAS is able to bind the main part of manganese previously bound to PAS, mainly as 1:1 complex.

When the total concentration of the ligand (as PAS + AcPAS) decreases up to 1/100 of the starting value, AcPAS ligand becomes the principal chelating agent and binds about 80% of manganese when the ratio [AcPAS]/[PAS] becomes = 1. As the concentration of PAS and AcPAS ligands decreases at 1/1000 of the starting value (as can realistically be in the brain), the percent of the formed MnAcPAS complex drastically reduces.

The plots relative to higher manganese burden (lower figures) show exactly the same trend of those relative to the lower manganese burden, and this depends on the fact that the ligands are always in large excess with respect to the metal.

3.5. Cellular Assay

The T98G cells in culture plates were growing with medium of Mn^{2+} concentration 0 (control sample), 113, 284, 566 and 1125 µM. After 24 h, morphological changes in cell cultures were observed and the viability was lowered until 40% (samples containing Mn^{2+} 566 and 1125 µM) respect to control sample (viability 90%). The 990 µM concentration of Mn^{2+} ions was chosen for further experiments.
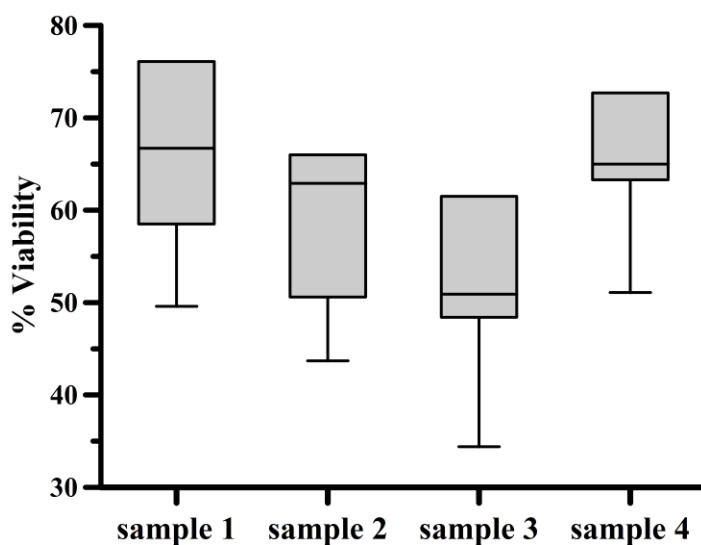

Figure 13. Box-whisker plot of the % viability of the T98G cells at the end of the experiment.

The two samples (sample 1 and 2) were growing in the absence of Mn^{2+} ions, while other 2 samples (sample 3 and 4) were growing in the presence of Mn^{2+} 990 µM for 24h. After 24h all the samples were washed with phosphate buffered saline solution (PBS solution) and fresh cell growing medium was added. Successively PAS solution was added to the samples 2 and 4 to the final concentration 78 µM. After 24 h the cell vailability was counted with Luna-FL™ Cell counter (5 counts for each sample). Figure 14 shows the viability of the cell cultures at the end of the experiment.

We can observe that the presence of PAS (Sample 2) for 24 h decrease the % viability in these cell cultures conditions. The presence of Mn^{2+} ions for 24 h (Sample 3) decreases the % cells' viability to the 50% (medium value) and lead to the morphological changes of the cells observable with optical microscope. The cells growing 24 h with Mn^{2+} ions and then 24 h with PAS (Sample 4) show an increased rate of the % viability (compare to sample 1) and a control sample comparable morphology (Sample 1).

Conclusions

A number of complementary experimental techniques and DFT calculations have been used in this paper for a thorough comprehension of protonation of PAS and Ac-PAS and their complex formation equilibria with the target Mn^{2+} ion, leading to the 1:1 and 1:2 metal:ligand complex formation. Surprisingly the N-acetylated metabolite forms stronger complexes, whose implications in chelation therapy is documented in the present paper. It is presumed that the Ac-PAS relatively small molecule is able to penetrate across the blood-to-brain border and exert its Mn-mobilizing action intracellularly in vulnerable neurons. Thereby, it transports the neurotoxic metal from vulnerable sites into circulating blood. Ac-PAS may also have an anti-inflammatory action intracellularly in brain. It is reasonable to suggest that the Mn-mobilizing action exerted by Ac-PAS ligand can be enhanced by a combined therapy with an extracellularly acting chelator, e.g. CaEDTA that rapidly escorts the metal into urine.

Acknowledgements

References

[1]   Martin, R.B.; Seiler, H.G.; Sigel, H.; Sigel, A.; Marcel-Dekker, Handbook on toxicity of inorganic compounds, New York, **1988**.

[2]   Keen, C.L.; Ensunsa, J.L.; Clegg, M.S., Manganese metabolism in animals and humans including the toxicity of manganese. *Metal Ions in Biological Systems,* **2000**, *37*, 89-121.

[3]   Freeland-Graves, J.H.; Turnlund, J.R., Deliberations and evaluations of the approaches, endpoints and paradigms for manganese and molybdenum dietary recommendations. *The Journal of Nutrition,* **1996**, *126*, (9), 2435S.

[4]   Wedler, F.C.; Denman, R.B., Glutamine synthetase: the major Mn (II) enzyme in mammalian brain. *Current topics in cellular regulation,* **1983**, *24*, 153-169.

[5]   Dorman, D.C.; Struve, M.F.; Clewell, H.J.; Andersen, M.E., Application of pharmacokinetic data to the risk assessment of inhaled manganese. *Neurotoxicology,* **2006**, *27*, (5), 752-764.

[6]   Crossgrove, J.; Zheng, W., Manganese toxicity upon overexposure. *NMR in Biomedicine,* **2004**, *17*, (8), 544-553.

[7]   Kim, E.A.; Cheong, H.K.; Choi, D.S.; Sakong, J.; Ryoo, J.W.; Park, I.; Kang, D.M., Effect of occupational manganese exposure on the central nervous system of welders: 1 H magnetic resonance spectroscopy and MRI findings. *Neurotoxicology,* **2007**, *28*, (2), 276-283.

[8]   Andersen, O., Chelation Treatment During Acute and Chronic MetalOverexposures—Experimentaland Clinical Studies, In *Chelation Therapy in the Treatment of Metal Intoxication*; Aaseth, J., Crisponi, G., Andersen, O. Eds., Elsevier Science, **2016**.

[9]   Ky, S.Q.; Deng, H.S.; Xie, P.Y.; Hu, W., A report of two cases of chronic serious manganese poisoning treated with sodium para-aminosalicylic acid. *British Journal of Industrial Medicine,* **1992**, *49*, (1), 66-69.

[10]   Jiang, Y.M.; Mo, X.A.; Du, F.Q.; Fu, X.; Zhu, X.Y.; Gao, H.Y.; Xie, J.L.; Liao, F.L.; Pira, E.; Zheng, W., Effective treatment of manganese-induced occupational Parkinsonism with p-aminosalicylic acid: a case of 17-year follow-up study. *Journal of Occupational and Environmental Medicine/American College of Occupational and Environmental Medicine,* **2006**, *48*, (6), 644.

[11]   Peloquin, C.A.; Zhu, M.; Adam, R.D.; Singleton, M.D.; Nix, D.E., Pharmacokinetics of para-aminosalicylic acid granules under four dosing conditions. *Annals of Pharmacotherapy,* **2001**, *35*, (11), 1332-1338.

[12]   Hong, L.; Jiang, W.; Pan, H.; Jiang, Y.; Zeng, S.; Zheng, W., Brain regional pharmacokinetics of p-aminosalicylic acid and its N-acetylated metabolite: effectiveness in chelating brain manganese. *Drug Metabolism and Disposition,* **2011**, *39*, (10), 1904-1909.

[13]   Zheng, W.; Jiang, Y.M.; Zhang, Y.; Jiang, W.; Wang, X.; Cowan, D.M., Chelation therapy of manganese intoxication with para-aminosalicylic acid (PAS) in Sprague–Dawley rats. *Neurotoxicology,* **2009**, *30*, (2), 240-248.

[14]   Bade, A.N.; Zhou, B.; McMillan, J.; Narayanasamy, P.; Veerubhotla, R.; Gendelman, H.E.; Boska, M.D.; Liu, Y., Potential of N-acetylated-para-aminosalicylic acid to accelerate manganese enhancement decline for long-term MEMRI in rodent brain. *Journal of Neuroscience Methods,* **2015**, *251*, 92-98.

[15]   Gran, G., Determination of equivalence point in potentiometric titrations. *Analyst,* **1952**, *77*, 661-671.

[16]   Willi, A.; Stocker, J., Kinetik der Decarboxylierung von p-Aminosalicylsäure. *Helvetica Chimica Acta,* **1954**, *37*, (4), 1113-1121.

[17]   Gans, P.; Sabatini, A.; Vacca, A., Investigation of equilibria in solution. Determination of equilibrium constants with the HYPERQUAD suite of programs. *Talanta,* **1996**, *43*, (10), 1739-1753.

[18]   Lachowicz, J.I.; Nurchi, V.M.; Crisponi, G.; Jaraquemada-Pelaez, M.; Arca, M.; Pintus, A.; Santos, M.; Quintanova, C.; Gano, L.; Szewczuk, Z., Hydroxypyridinones with enhanced iron chelating properties. Synthesis, characterization and in vivo tests of 5-hydroxy-2-(hydroxymethyl) pyridine-4 (1 H)-one. *Dalton Transactions,* **2016**, *45*, (15), 6517-6528.

[19]   Gans, P.; Sabatini, A.; Vacca, A., Determination of equilibrium constants from spectrophometric data obtained from solutions of known pH: The program pHab. *Annali di Chimica,* **1999**, *89*, (1-2), 45-49.

[20]   Yanai, T.; Tew, D.P.; Handy, N.C., A new hybrid exchange–correlation functional using the Coulomb-attenuating method (CAM-B3LYP). *Chemical Physics Letters,* **2004**, *393*, (1), 51-57.

[21]   Guo, H.-B.; He, F.; Gu, B.; Liang, L.; Smith, J.C., Time-dependent density functional theory assessment of UV absorption of benzoic acid derivatives. *The Journal of Physical Chemistry A,* **2012**, *116*, (48), 11870-11879.

[22]   Nurchi, V.M.; Crisponi, G.; Lachowicz, J.I.; Zoroddu, M.A.; Peana, M.; Medici, S.; Veclani, D.; Tolazzi, M.; Melchior, A., Fluoroquinolones: A micro-species equilibrium in the protonation of amphoteric compounds. *European Journal of Pharmaceutical Sciences,* **2016**, *93*, 380-391.

[23]   Tomasi, J.; Mennucci, B.; Cammi, R., Quantum mechanical continuum solvation models. *Chemical Reviews,* **2005**, *105*, (8), 2999-3094.

[24]   Becke, A.D., A new mixing of Hartree–Fock and local density-functional theories. *The Journal of Chemical Physics,* **1993**, *98*, (2), 1372-1377.

[25]   Lee, C.; Yang, W.; Parr, R.G., Development of the Colle-Salvetti correlation-energy formula into a functional of the electron density. *Physical Review B,* **1988**, *37*, (2), 785.

[26]   Melchior, A.; Gaillard, C.; Gràcia Lanas, S.; Tolazzi, M.; Billard, I.; Georg, S.; Sarrasin, L.; Boltoeva, M., Nickel (II) Complexation with Nitrate in Dry [C4mim][Tf2N] Ionic Liquid: A Spectroscopic, Microcalorimetric, and Molecular Dynamics Study. *Inorganic Chemistry,* **2016**, *55*, (7), 3498-3507.

[27]   Del Piero, S.; Di Bernardo, P.; Fedele, R.; Melchior, A.; Polese, P.; Tolazzi, M., Affinity of polypyridines towards CdII and CoII ions: a thermodynamic and DFT study. *European Journal of Inorganic Chemistry,* **2006**, *2006*, (18), 3738-3745.

[28]   Di Bernardo, P.; Zanonato, P.L.; Benetollo, F.; Melchior, A.; Tolazzi, M.; Rao, L., Energetics and Structure of Uranium (VI)–Acetate Complexes in Dimethyl Sulfoxide. *Inorganic Chemistry,* **2012**, *51*, (16), 9045-9055.

[29]   Melchior, A.; Peralta, E.; Valiente, M.; Tavagnacco, C.; Endrizzi, F.; Tolazzi, M., Interaction of d 10 metal ions with thioether ligands: a thermodynamic and theoretical study. *Dalton Transactions,* **2013**, *42*, (17), 6074-6082.

[30]   Ojamäe, L.; Hermansson, K., Water molecules in different crystal surroundings: Vibrational O–H frequencies from abinitio calculations. *The Journal of Chemical Physics,* **1992**, *96*, (12), 9035-9045.

[31]   Barone, V.; Cossi, M., Quantum calculation of molecular energies and energy gradients in solution by a conductor solvent model. *The Journal of Physical Chemistry A,* **1998**, *102*, (11), 1995-2001.

[32]   Cossi, M.; Rega, N.; Scalmani, G.; Barone, V., Energies, structures, and electronic properties of molecules in solution with the C-PCM solvation model. *Journal of Computational Chemistry,* **2003**, *24*, (6), 669-681.

[33]   Trzaskowski, B.; Les, A.; Adamowicz, L., Modelling of octahedral manganese II complexes with inorganic ligands: A problem with spin-states. *International Journal of Molecular Sciences,* **2003**, *4*, (8), 503-511.

[34]   van Gorkum, R.; Buda, F.; Kooijman, H.; Spek, A.L.; Bouwman, E.; Reedijk, J., Trigonal-Prismatic vs. Octahedral Geometry for MnII Complexes with Innocent Didentate Ligands: A Subtle Difference as Shown by XRD and DFT on [Mn (acac) 2 (bpy)]. *European Journal of Inorganic Chemistry,* **2005**, *2005*, (11), 2255-2261.

[35]   Mayer, I., Charge, bond order and valence in the ab initio SCF theory. *Chemical Physics Letters,* **1983**, *97*, (3), 270-274.

[36]   Bridgeman, A.J.; Cavigliasso, G.; Ireland, L.R.; Rothery, J., The Mayer bond order as a tool in inorganic chemistry. *Dalton Transactions,* **2001**, (14), 2095-2108.

[37]   Frisch, M.J.T., G. W.; Schlegel, H. B.; Scuseria, G. E.; Robb, M. A.; Cheeseman, J. R.; Scalmani, G.; Barone, V.; Mennucci, B.; Petersson, G. A.; Nakatsuji, H.; Caricato, M.; Li, X.; Hratchian, H. P.; Izmaylov, A. F.; Bloino, J.; Zheng, G.; Sonnenberg, J. L.; Hada, M.; Ehara, M.; Toyota, K.; Fukuda, R.; Hasegawa, J.; Ishida, M.; Nakajima, T.; Honda, Y.; Kitao, O.; Nakai, H.; Vreven, T.; Montgomery, J. A., Jr.; Peralta, J. E.; Ogliaro, F.; Bearpark, M.; Heyd, J. J.; Brothers, E.; Kudin, K. N.; Staroverov, V. N.; Kobayashi, R.; Normand, J.; Raghavachari, K.; Rendell, A.; Burant, J. C.; Iyengar, S. S.; Tomasi, J.; Cossi, M.; Rega, N.; Millam, J. M.; Klene, M.; Knox, J. E.; Cross, J. B.; Bakken, V.; Adamo, C.;

Jaramillo, J.; Gomperts, R.; Stratmann, R. E.; Yazyev, O.; Austin, A. J.; Cammi, R.; Pomelli, C.; Ochterski, J. W.; Martin, R. L.; Morokuma, K.; Zakrzewski, V. G.; Voth, G. A.; Salvador, P.; Dannenberg, J. J.; Dapprich, S.; Daniels, A. D.; Farkas, Ö.; Foresman, J. B.; Ortiz, J. V.; Cioslowski, J.; Fox, D. J. , Gaussian 09, Revision D.01, Gaussian, Inc. *Wallingford, CT,* **2009**.

[38]   Nurchi, V.M.; Crisponi, G.; Lachowicz, J.I.; Sanna, G.; Peana, M.; Zoroddu, M.A., Substituent effects on ionization constants as a predictive tool of coordinating ability. *Monatshefte für Chemie-Chemical Monthly,* **2016**, *147*, (4), 719-724.

[39]   Alderighi, L.; Gans, P.; Ienco, A.; Peters, D.; Sabatini, A.; Vacca, A., Hyperquad simulation and speciation (HySS): a utility program for the investigation of equilibria involving soluble and partially soluble species. *Coordination Chemistry Reviews,* **1999**, *184*, (1), 311-318.

[40]   Reed, G.; Poyner, R.; Dekker, Metal Ions in Biological Systems Siegel, A. and Siegel, H., eds New York, **2000**.

[41]   Reed, G.H.; Markham, G.D., EPR of Mn (II) complexes with enzymes and other proteins. *Biological Magnetic Resonance,* **1984**, *6*, 73-142.

[42]   Remelli, M.; Peana, M.; Medici, S.; Delogu, L.G.; Zoroddu, M.A., Interaction of divalent cations with peptide fragments from Parkinson's disease genes. *Dalton Transactions,* **2013**, *42*, (17), 5964-5974.

[43]   Peana, M.; Medici, S.; Pangburn, H.A.; Lamkin, T.J.; Ostrowska, M.; Gumienna-Kontecka, E.; Zoroddu, M.A., Manganese binding to antioxidant peptides involved in extreme radiation resistance in Deinococcus radiodurans. *Journal of Inorganic Biochemistry,* **2016**, *164*, 49-58.

[44]   Remelli, M.; Peana, M.; Medici, S.; Ostrowska, M.; Gumienna-Kontecka, E.; Zoroddu, M.A., Manganism and Parkinson's disease: Mn (II) and Zn (II) interaction with a 30-amino acid fragment. *Dalton Transactions,* **2016**, *45*, (12), 5151-5161.

[45]   Medici, S.; Peana, M.; Delogu, L.G.; Zoroddu, M.A., Mn (II) and Zn (II) interactions with peptide fragments from Parkinson's disease genes. *Dalton Transactions,* **2012**, *41*, (15), 4378-4388.

[46]   Hurd, F.K.; Sachs, M.; Hershberger, W., Paramagnetic Resonance Absorption of Mn^{++} in Single Crystals of $CaCO_3$. *Physical Review,* **1954**, *93*, (3), 373.

[47]   Mankowitz, J.; Low, W., Forbidden Transitions (Δ m=$\pm$1) in the Paramagnetic Resonance Absorption of Mn^{2+} in Calcite. *Physical Review B,* **1970**, *2*, (1), 28.

[48]   Eidels-Dubovoi, S.; Beltrán-López, V., Dependence on an axial crystal field of the Mn2+ EPR line intensities in powder samples. *Journal of Magnetic Resonance (1969),* **1978**, *32*, (3), 441-449.

[49]   Zhang, Y.; Buckmaster, H., The 9 and 33 GHz EPR Spectra of Mn2+ Impurity Ions in Polycrystalline Calcite-Noncentral Transitions. *Journal of Magnetic Resonance, Series A,* **1993**, *102*, (2), 151-159.

[50]   Shepherd, R.A.; Graham, W., EPR of Mn2+ in polycrystalline dolomite. *The Journal of Chemical Physics,* **1984**, *81*, (12), 6080-6084.

[51]   Garribba, E.; Micera, G., Determination of the hyperfine coupling constant and zero-field splitting in the ESR spectrum of Mn^{2+} in calcite. *Magnetic Resonance in Chemistry,* **2006**, *44*, (1), 11-19.

[52]   Sasmal, A.; Garribba, E.; Ugone, V.; Rizzoli, C.; Mitra, S., Synthesis, crystal structures, EPR and DFT studies of first row transition metal complexes of lignin model compound ethylvanillin. *Polyhedron,* **2017**, *121*, 107-114.

[53]   Baute, D.; Goldfarb, D., The 17O Hyperfine Interaction in V17O (H217O) 52+ and Mn (H217O) 62+ Determined by High Field ENDOR Aided by DFT Calculations. *The Journal of Physical Chemistry A,* **2005**, *109*, (35), 7865-7871.

[54]   Esteban-Gómez, D.; Cassino, C.; Botta, M.; Platas-Iglesias, C., 17 O and 1 H relaxometric and DFT study of hyperfine coupling constants in $[Mn(H_2O)6]^{2+}$. *RSC Advances,* **2014**, *4*, (14), 7094-7103.

[55]   Endrizzi, F.; Melchior, A.; Tolazzi, M.; Rao, L., Complexation of uranium (VI) with glutarimidoxioxime: thermodynamic and computational studies. *Dalton Transactions,* **2015**, *44*, (31), 13835-13844.

[56]   Melchior, A.; Marcos, E.S.; Pappalardo, R.R.; Martínez, J.M., Comparative study of the hydrolysis of a third-and a first-generation platinum anticancer complexes. *Theoretical Chemistry Accounts,* **2011**, *128*, (4-6), 627-638.

[57]   Melchior, A.; Tolazzi, M.; Martínez, J.M.; Pappalardo, R.R.; Sánchez Marcos, E., Hydration of two cisplatin aqua-derivatives studied by quantum mechanics and molecular dynamics simulations. *Journal of Chemical Theory and Computation,* **2015**, *11*, (4), 1735-1744.

[58]   Peisach, J.; Blumberg, W., Structural implications derived from the analysis of electron paramagnetic resonance spectra of natural and artificial copper proteins. *Archives of Biochemistry and Biophysics,* **1974**, *165*, (2), 691-708.

[59]   Hathaway, B.; Billing, D., The electronic properties and stereochemistry of mono-nuclear complexes of the copper (II) ion. *Coordination Chemistry Reviews,* **1970**, *5*, (2), 143-207.

[60]   Garribba, E.; Micera, G., The determination of the geometry of Cu(II) complexes: an EPR spectroscopy experiment. *Journal of Chemical Education,* **2006**, *83*, (8), 1229.